Pre-steady-state kinetic studies of redox reactions catalysed by Bacillus subtilis ferredoxin-NADP+ oxidoreductase with NADP+/NADPH and ferredoxin

Title

Pre-steady-state kinetic studies of redox reactions catalysed by *Bacillus subtilis* ferredoxin-$NADP^+$ oxidoreductase with $NADP^+$/NADPH and ferredoxin

Authors

Daisuke Seo[a*], Takahiro Soeta[a], Hidehiro Sakurai[b], Pierre Sétif[c,d], Takeshi Sakurai[a]

Address

[a]Division of Material Science, Graduate School of Natural Science and Technology, Kanazawa University, Kakuma, Kanazawa, Ishikawa 920-1192, Japan

[b]Research Institute for Photobiological Hydrogen Production, Kanagawa University, Tsuchiya, Hiratsuka, Kanagawa 259-1293, Japan

[c]CEA, iBiTecS, 91191 Gif sur Yvette, France

[d]CNRS/Université Paris-Sud/CEA, I2BC, 91190 Gif sur Yvette, France

*****Corresponding author: Division of Material Science, Graduate School of Natural Science and Technology, Kanazawa University, Kakuma, Kanazawa, Ishikawa 920-1192, Japan

Tel: +81-76-264-5683

Fax: +81-76-264-5742

e-mail: dseo@se.kanazawa-u.ac.jp

Abbreviations

Ad, adrenodoxin; AdR, adrenodoxin reductase; *An*, *Anabaena*; *Bs*, *Bacillus subtilis*; *Ct*, *Chlorobaculum tepidum*; CT, charge transfer; CTC, charge transfer complex; *Ec*, *Escherichia coli*; dRf, 5-deazariboflavin; FAD, flavin-adenine dinucleotide; Fd, ferredoxin; Fld, flavodoxin; FNR, ferredoxin-$NAD(P)^+$ oxidoreductase; GR, glutathione reductase; HEPES, 2-[4-(2-hydroxyethyl)-1-piperazinyl]ethanesulphonic acid; MC, Michaelis complex; NADPD, (4S-^{2}H)-reduced nicotinamide adenine dinucleotide phosphate; Pd, putidaredoxin; PdR, putidaredoxin reductase; PSI, photosystem I; TrxR, bacterial NADPH-thioredoxin reductase; *Tt*, *Thermus thermophilus*

Suffixes: ox, oxidized; red, reduced; sq, semiquinone

Abstract

Ferredoxin-$NADP^+$ oxidoreductase ([EC1.18.1.2], FNR) from *Bacillus subtilis* (*Bs*FNR) is a homodimeric flavoprotein sharing structural homology with bacterial NADPH-thioredoxin reductase. Pre-steady-state kinetics of the reactions of *Bs*FNR with $NADP^+$, NADPH, NADPD (deuterated form) and *B. subtilis* ferredoxin (*Bs*Fd) using stopped-flow spectrophotometry were studied. Mixing *Bs*FNR with $NADP^+$ and NADPH yielded two types of charge-transfer (CT) complexes, oxidized FNR (FNR_{ox})-NADPH and reduced FNR (FNR_{red})-$NADP^+$, both having CT absorption bands centered at approximately 600 nm. After mixing *Bs*FNR_{ox} with about a 10-fold molar excess of NADPH (forward reaction), *Bs*FNR was almost completely reduced at equilibrium. When *Bs*FNR_{red} was mixed with $NADP^+$, the amount of *Bs*FNR_{ox} increased with increasing $NADP^+$ concentration, but *Bs*FNR_{red} remained as the major species at equilibrium even with about 50-fold molar excess $NADP^+$. In both directions, the hydride-transfer was the rate-determining step, where the forward direction rate constant (~500 s^{-1}) was much higher than the reverse one (< 10 s^{-1}). Mixing *Bs*Fd_{red} with *Bs*FNR_{ox} induced rapid formation of a neutral semiquinone form. This process was almost completed within 1 ms. Subsequently the neutral semiquinone form was reduced to the hydroquinone form with an apparent rate constant of 50 to 70 s^{-1} at 10°C, which increased as *Bs*Fd_{red} increased from 40 to 120 μM. The reduction rate of *Bs*FNR_{ox} by *Bs*Fd_{red} was markedly decreased by premixing *Bs*FNR_{ox} with *Bs*Fd_{ox}, indicating that the dissociation of *Bs*Fd_{ox} from *Bs*FNR_{sq} is rate-limiting in the reaction. The characteristics of the *Bs*FNR reactions with $NADP^+$/NADPH were compared with those of other types of FNRs.

Keywords

ferredoxin; flavodoxin; *Bacillus*; adrenodoxin; putidaredoxin; *yumC*

1. Introduction

The low-molecular-weight iron sulfur proteins ferredoxin (Fd), adrenodoxin (Ad) and putidaredoxin (Pd) serve as low to moderate reduction/oxidation (redox) potential one-electron carriers in a variety of biological processes, such as carbon dioxide and sulfur assimilation, nitrogen fixation, cytochrome P450-dependent hydroxylase reactions and S-adenosylmethionine-dependent reactions [1–7]. In many non-photosynthetic organisms and tissues, Fd-NAD(P)$^+$ oxidoreductase ([EC 1.18.1.2], [EC1.18.1.3], FNR), adrenodoxin reductase ([EC 1.18.1.6], AdR) and putidaredoxin reductase ([EC 1.18.1.5], PdR) as well as their homologues in several bacteria [8–12] reduce Fd, Ad and Pd with NAD(P)H. FNR, AdR and PdR belong to the flavoprotein superfamily. Most contain a non-covalently bound flavin-adenine dinucleotide (FAD) as the prosthetic group, while a few have a flavin mononucleotide. Based on their amino acid sequence homologies and 3D structure analyses, they are divided into two major groups, the plant-type and the glutathione reductase (GR)-type FNR superfamilies [13–19]. The bacterial NADPH-thioredoxin reductase (TrxR)-type FNR, a subfamily of the GR-type FNR superfamily, was first isolated from the photoautotrophic green sulfur bacterium *Chlorobaculum tepidum* (*Ct*) [20]. This type of FNR was then purified in native and recombinant forms from various bacteria such as the low-GC gram-positive bacterium *Bacillus subtilis* (*Bs*), the purple non-sulfur bacterium *Rhodopseudomonas palstris*, the extreme thermophile *Thermus thermophilus* (*Tt*) and the hyper-thermophilic archaeon *Sulfolobus tokodaii* [17–19, 21–22]. Most TrxR-type FNRs occur as homodimers in solution, whereas plant-type and other GR-type FNRs generally occur and function as monomers. Recent X-ray crystallographic studies of *Ct*FNR (PDB code: 3AB1), *Tt*FNR (PDB code: 2ZBW) and *Bs*FNR (PDB code: 3LZX, 3LZW) revealed that these FNRs share a folding topology in the polypeptide main chain with TrxR from *Escherichia coli* (*Ec*TrxR) [19, 23, 24]. In the crystal structure of *Bs*FNR and *Ct*FNR, the *re*-face of the isoalloxazine ring of the FAD is covered by the extended C-terminal region from the other protomer, and the two aromatic residues are stacked on the *si*- and *re*-faces of the ring at a distance of 3–4 Å where the direct access of the NADPH-binding domain to the isoalloxazine ring is prevented [19, 23]. In *Ec*TrxR, the corresponding aromatic residues and extended C-terminal region are absent, and the NADPH-binding domain can directly access the *re*-face of the isoalloxazine ring [24, 25],

indicating the differences in NADPH accessing mode to the *re*-face of the isoalloxazine ring between *Ec*TrxR and TrxR-type FNRs.

In general, redox reactions between FNRs and the two-electron carrier nucleotides $NAD(P)^+$/NAD(P)H proceed by hydride transfer via the formation of two types of charge-transfer complexes (CTCs), namely the FNR_{ox}-NADPH complex (CTC-1) and FNR_{red}-$NADP^+$ complex (CTC-2). Both CTCs are characterized by the typical charge-transfer (CT) absorption band(s) in the 500–800 nm region, similar to many enzymes in flavin-dependent NAD(P)H oxidoreductase families [26, 27]. Pre-steady-state studies of plastid-type FNRs [27, 28], the GR-type FNR from *Mycobacterium tuberculosis* [29] and *Ec*TrxR [30] with NAD(P)H have shown that the reaction of oxidized enzymes with NAD(P)H involves the rapid formation of CTCs, as demonstrated by the appearance of an absorption band in the longer wavelength (>500 nm) region, followed by a rate-limiting hydride transfer. From kinetic studies, the formation of Michaelis complexes (MCs) has been identified in *Ec*TrxR, plant-type FNR and several other related enzymes, although no unique absorption spectra have been assigned to MC-1 and MC-2 [2, 27, 30]. The reaction sequences involving MCs and CTCs can be represented schematically, as shown in Scheme 1.

$$\underset{}{FNR_{ox}} + NADPH \underset{k_{-1}}{\overset{k_{+1}}{\rightleftharpoons}} \underset{\text{MC-1}}{FNR_{ox}\_NADPH} \underset{k_{-2}}{\overset{k_{+2}}{\rightleftharpoons}} \underset{\text{CTC-1}}{FNR_{ox}\text{-}NADPH} \underset{k_{-3}}{\overset{k_{+3}}{\rightleftharpoons}} \underset{\text{CTC-2}}{FNR_{red}\text{-}NADP^+} \underset{k_{-4}}{\overset{k_{+4}}{\rightleftharpoons}} \underset{\text{MC-2}}{FNR_{red}\_NADP^+} \underset{k_{-5}}{\overset{k_{+5}}{\rightleftharpoons}} FNR_{red} + NADP^+$$

Scheme 1

The redox reaction between FNR and the one-electron carrier protein Fd involves two consecutive one-electron transfer steps, leading to the formation of the three different redox states of FAD, i.e. the fully oxidized quinone state (FNR_{ox}), the one-electron reduced semiquinone state (FNR_{sq}), and the fully reduced hydroquinone state (FNR_{red}). Their appropriate redox properties are essential for optimizing the direction of electron transfer in accordance with their physiological functions. The pre-steady-state kinetics of AdR [31], PdR [32, 33] and plastid-type FNRs [34-38] with the one-electron carrier Fd, either in the oxidized form or in the reduced form, have been frequently studied spectroscopically. Studies of the *Anabaena* (*An*) PCC7119 plastid-type FNR-Fd system showed that the reaction between photochemically reduced Fd (Fd_{red}) and FNR_{ox} yields a second-order rate constant corresponding to Fd_{red}–FNR_{ox} complex formation of ~1×10^8 M^{-1} s^{-1} and a rate constant corresponding to the subsequent internal electron-

transfer process in a competent Fd_{red}-FNR_{ox} complex of ~5,500 s^{-1} at 23°C–25°C [37, 38]. In studies of the reconstituted $NADP^+$-photoreduction system of *Synechocystis* PCC6803 comprised PSI, Fd, and FNR, the second-order rate constant for the reduction of the plastid-type FNR_{ox} by Fd_{red} was found to be 3–6 × 10^8 $M^{-1}s^{-1}$ with a turnover rate of ~400 electrons per second and per FNR [34]. The results obtained from these pre-steady-state kinetic studies indicate that the formation of the competent Fd–FNR complex and the following internal electron transfer both occur rapidly, and that the overall turnover rate is determined largely by other steps. Previous comprehensive studies of the plastid-type FNR using stopped-flow spectrophotometry by Batie and Kamin ([2, 28] and the references therein) found that the rate-limiting step in the reaction is the dissociation of Fd_{ox} from FNR_{sq}.

In contrast to the other FNR members, the spectroscopic and kinetic details of the TrxR-type FNR catalyzed reaction has not been reported yet. In the previous steady-state studies [21], the reduction of *Bs*FNR with NADPH yielded absorption bands at approximately 600 nm, which was assigned to the formation of CTCs. In contrast to the other NAD(P)H-dependent oxidoreductases, no absorption bands were observed with peaks beyond 700 nm. The studies of electron donation by *Bs*Fd and *Bs*Flds in cytochrome P450-dependent reactions and the NO synthase reaction support the physiological role of *Bs*Fd as the electron donor to these enzymes [39–42]. In steady-state studies, *Bs*FNR was found to reduce *Bs*Fd (E_{m7} = −385 mV, [39]) with NADPH at a relatively high rate (~50 s^{-1}) [43], but the rate decreased as the NADPH concentration increased, indicating substrate inhibition. In the present study, we performed pre-steady-state studies of the redox reactions between *Bs*FNR and $NADP^+$, NADPH, (4S-^{2}H)-reduced nicotinamide adenine dinucleotide phosphate ((4S-^{2}H)-NADPD) or *Bs*Fd using stopped-flow spectrophotometry to elucidate the kinetics of the elementary reactions in more detail.

2. Materials and Methods

2.1 Preparations of BsFNR and BsFd

Wild-type *Bs*FNR was overexpressed in *Escherichia coli* cells and purified according to the previously described method [43]. The expression and purification of *Bs*Fd were performed as described previously [21, 43].

2.2 Pre-steady-state reaction analysis with stopped-flow spectrophotometry

Stopped-flow spectrophotometry was performed in a glove box under a N_2 atmosphere containing H_2 gas (ca. 5%) to reduce the residual O_2 to less than 50 ppm with a palladium catalyst. The stopped-flow spectrophotometer system comprised a temperature-controlled double mixing unit (USP-SFM-D20, Unisoku Co., Ltd, Osaka, Japan) with a micro-volume cell (1 mm diameter window and 1 cm light path length), a 150 W xenon discharge lamp house (USP-105-04, Unisoku Co., Ltd) with a color-compensating filter (MC FL-W, Kenko Tokina Co., Ltd, Tokyo, Japan), and a photodiode array detector (PK120, Unisoku Co., Ltd). The mixing unit inside the glove box was connected by quartz light guides to the lamp house and the detector outside the glove box. The reaction was initiated by mixing equal volumes of solutions in a single mixing mode at 10°C. Spectra were collected every 1 ms after stopping the piston motion. Using 0.1 mM dichlorophenol indophenol and 1–10 mM sodium ascorbate solution at pH 2.0 [44, 45], mixing was >95% complete within 1 ms (Fig. S1). In the present paper with the exception of Fig.S1, 1 ms was subtracted from the data acquisition time to compensate for the time required for stopping the flow of the solution after stopping the piston motion.

All of the protein and substrate concentrations are given as the final concentrations after mixing unless stated otherwise. Photoreduction of *Bs*FNR was performed according to the previously described method with minor modifications [27, 46]. Briefly, 40–100 μM FNR solution in 20 mM 2-[4-(2-hydroxyethyl)-1-piperazinyl]ethanesulphonic acid (HEPES)-NaOH buffer (pH 7.0) containing 1.2 μM dRf and 2 mM EDTA was irradiated in the glove box by a 150-W xenon discharge lamp (XEF-152S, Kenko Tokina Co., Ltd) through a light guide. Absorption spectra were monitored during photoreduction using a photodiode array spectrophotometer

(BRC741E, B&W Tek, Inc., Newark, DE, USA) with a halogen light source. O_2 was removed from the buffers, protein solutions and reagents beforehand by more than five cycles of evacuation and purging with pure argon gas.

BsFd_{red} was prepared via the stepwise addition of a sodium dithionite solution (typically approximately 90 μl of 4 mg ml^{-1} sodium dithionite solution to 4.5 ml of 400 μM *Bs*Fd solution) in the glove box while monitoring the absorption spectra with a photodiode array spectrophotometer (BRC741E, B&W Tek, Inc.) to ensure the complete reduction [28, 47].

Protein and substrate concentrations were determined from the extinction coefficients: *Bs*FNR_{ox} ε_{457} = 12.3 mM^{-1} cm^{-1} [17], *Bs*Fd_{ox} ε_{390} = 16.0 mM^{-1} cm^{-1} [39] and NADPH/(4S-^{2}H)-NADPD ε_{340} = 6.2 mM^{-1} cm^{-1}. $NADP^+$ and NADPH were purchased from Oriental Yeast Co., Ltd (Tokyo, Japan). Synthetic dRf was prepared according to previously described methods [48]. The dRf concentration was determined based on its extinction coefficient of 12.5 mM^{-1} cm^{-1} at 397 nm [49].

The values of A_{458}, A_{590}, ε_{458} and ε_{590} in Figures 1 to 3 were obtained by subtracting A_{800} to compensate for a signal drift.

2.3 Kinetic data analysis

Data collection and basic arithmetic operations on the transient spectra obtained from stopped-flow experiments were performed using Unispec (ver. 2.51, Unisoku Co., Ltd) and Excel (ver. 14 and 15, Microsoft Corporation, Redmond, WA, USA) software. The kinetic simulations with reversible redox reactions represented in Schemes 1 and 2 were performed using COPASI ver. 4.11 software [50]. Details of the kinetic simulations are described in the Supplemental Materials. Curve fitting to the transient absorptions at a single wavelength was performed using Igor Pro ver. 6.3 software (Wavemetrics, Portland, OR, USA).

2.4 Miscellaneous methods

The semiquinone spectrum of *Bs*FNR was obtained by mixing 50 μM photoreduced *Bs*FNR with 5 μM potassium ferricyanide in the stopped-flow spectrophotometer to minimize the formation of fully oxidized *Bs*FNR to a negligible level.

The spectra of $BsFd_{ox}$ and $BsFd_{red}$ were measured under anaerobic conditions. $BsFd_{red}$ was obtained by adding a slight excess of sodium dithionite (~10-fold) in 20 mM HEPES-NaOH buffer (pH 7.0) at room temperature.

The deuterated form (4*S*-^{2}H)-NADPD (referred to hereafter as NADPD) was prepared according to the methods in [51–53], as follows. Briefly, 35 mg $NADP^{+}$ was deuterated in the presence of 100 U glucose-6-phosphate dehydrogenase from yeast (Oriental Yeast Co., Ltd) and 15 mg D-glucose-1-^{2}H (Santa Cruz Biotechnology, TX, USA) in 4.2 ml of 50 mM potassium phosphate buffer (pH 8.0) containing 40% dimethyl sulfoxide at room temperature. After the increase in A_{340} was nearly complete (~3 h), the reaction mixture was subjected to ultrafiltration (10,000 MW cut off) to remove the enzyme, diluted with 10 mM ammonium bicarbonate solution (pH 10) and applied to a DEAE-5PW column (Tosoh Corporation, Tokyo, Japan), which had been pre-equilibrated with the same solution. After washing with one column volume of the same solution, NADPD was eluted with four column volumes of a linear gradient of 10–500 mM ammonium bicarbonate. Fractions with the ratio of $A_{260}/A_{340} < 2.7$ were collected and lyophilized, then the resultant residues were dissolved in 10 mM tris(hydroxymethyl)-aminomethane solution (pH 8.0) and stored at –80°C until use. The final A_{260}/A_{340} ratio of the NADPD solution thus obtained was 2.5.

3. Results

3.1 Kinetics of the redox reaction between BsFNR and $NADP^+$/NADPH

3.1.1 Reaction of $BsFNR_{ox}$ with NADPH

The forward reaction (reduction of *Bs*FNR_{ox} with NADPH) was performed by mixing 12 μM *Bs*FNR_{ox} with 100–500 μM NADPH. The rapid mixing with NADPH caused a decrease in absorbance in the flavin absorption band I region (400–500 nm) with a peak at approximately 460 nm, accompanied by the appearance of a broad absorption band centered at 600 nm (CT absorption band region) within the dead time (1 ms) (Fig. 1a). In the flavin absorption band I region, the absorbance initially dropped rapidly within 10 ms to almost the minimum level (Fig. 1a). The absorption in the CT absorption band region rapidly increased to the maximum intensity within 1 ms at NADPH concentrations between 100 and 500 μM followed by a rapid decrease until about 10 ms with a time constant similar to that of the decay of the flavin absorption band I region (A_{458}) at the NADPH concentration used (Fig. 1a, b insets). The subsequent decrease in the CT absorption band region was much slower (inset in Fig. 1a).

Figure 1b shows the time course of the A_{458} after mixing *Bs*FNR_{ox} with different concentrations of NADPH. The difference in the absorbance during the first data acquisition period of 1 ms (expressed as time 0 in Fig. 1b) was slightly affected by NADPH concentrations of 100, 200 and 500 μM (Fig. 1b). After 10 ms, the amount of *Bs*FNR_{red} was only slightly affected by the NADPH concentration in this range, indicating that the equilibrium was not greatly affected by the NADPH concentration used. The changes in observed A_{458} minus A_{458} of *Bs*FNR_{red} can be approximated to a single step reaction model as shown in the inset of Figure 1b, and the rate constant k_{obs} for this phase was estimated to be ~500 s^{-1} (Fig. 1b).

3.1.2 Reaction of $BsFNR_{ox}$ with NADPD

The primary kinetic isotope effect was examined using NADPD in place of NADPH in the forward reaction (Fig. 2) [54–57]. Mixing 10 μM *Bs*FNR_{ox} with NADPD caused a decrease in the absorbance in the flavin absorption band I region (Fig. 2a), but the rate of the decrease after 0 ms was much slower than that with NADPH (Fig. 1a). The absorbance of the CT absorption band region increased rapidly within 1 ms (Fig. 2a), similar to what was observed

with NADPH (Fig. 1a), but the rate of the subsequent decrease (Fig. 2a inset) was much slower than with NADPH (Fig. 1a inset). The slow changes that followed in the A_{458} after 0 ms were not significantly affected by the NADPD concentration from 100 to 500 μM (Fig. 2b). The changes in observed A_{458} minus A_{458} of *Bs*FNR$_{red}$ can be approximated to a single step reaction model, as shown in Figure 2b. The apparent rate constant k_{obs} for this phase was estimated to be ~50 s^{-1} (Fig. 2b), resulting in the kinetic isotope effect value ($k_{obs\ (NADPH)}$ /$k_{obs\ (NADPD)}$) of ~10.

To trace the changes of the amounts of CTC-1 and CTC-2 during the NADPH and NADPD oxidation reactions, the respective transitions of ε_{458} vs. ε_{590} were plotted in Figure 2c. The decay of CTC-1 decreases both ε_{458} and ε_{590} values, which was estimated as the dotted line in Figure 2c, whereas the change in CTC-2's amount only affected the ε_{590} value. Thus the difference between the dotted line and the data points indicates the amount of CTC-2. In Figure 2c, both NADPH and NADPD oxidation reactions provided almost parallel traces as shown by the dotted line, indicating that the amount of CTC-2 was almost constant during the reactions over the time period.

3.1.3 Reaction of BsFNR$_{red}$ with NADP$^+$

To study the reverse reaction (oxidation of *Bs*FNR$_{red}$ by NADP$^+$), *Bs*FNR$_{red}$ was prepared photochemically under continuous illumination in the presence of dRf, EDTA and *Bs*FNR$_{ox}$ (Fig. 3a). Mixing *Bs*FNR$_{red}$ (9 μM) with NADP$^+$ rapidly yielded a broad absorption band centered at 600 nm (CT absorption band region) with almost no increase in the absorption of the flavin absorption band I at 0 ms (Fig. 3b and c). The absorbance in the CT band region almost reached the maximum at 0 ms and did not noticeably change over the subsequent time range (30–480 ms) (Fig. 3b and c). The magnitude of the CT absorption band region was not significantly affected by NADP$^+$ concentrations from 100 to 500 μM (Fig. 3b and c). The absorption of the flavin absorption band I region gradually increased with time. The total change of A_{458} at 1000 ms were affected by NADP$^+$ concentration, but even in the presence of more than 50-fold molar excess NADP$^+$, more than half of *Bs*FNR remained as the reduced form (Fig. 3c). These results indicate that the redox potential of *Bs*FNR in the presence of 100–500 μM NADP$^+$/NADPH is significantly more positive than that of NADP$^+$/NADPH. The increase in A_{458} could be approximated by a single step reaction model, where its apparent rate constant decreased as the NADP$^+$ concentration increased (Fig. 3d and e).

3.2 Kinetics of BsFNR reduction by reduced BsFd

We studied the redox reaction between *Bs*FNR and the one-electron carrier *Bs*Fd by monitoring the transient spectra generated by the rapid mixing of $Bs\text{Fd}_{red}$ (40–120 μM) with $Bs\text{FNR}_{ox}$ (10 μM) in the visible to near-infrared region (Fig. 4). $Bs\text{Fd}_{red}$ was prepared in the glove box by successive additions of small amounts of sodium dithionite. The rate of the direct reduction of $Bs\text{FNR}_{ox}$ by dithionite (~1 mM) was very slow because no significant spectral changes were observed within a few seconds (data not shown).

In an effort to better understand the redox state of *Bs*FNR after mixing with $Bs\text{Fd}_{red}$ (Fig. S2a), the absorption spectrum of $Bs\text{Fd}_{red}$ in 20 mM HEPES-NaOH buffer (pH 7.0) was subtracted from each transient spectrum (Fig. 4a). Although the oxidation of $Bs\text{Fd}_{red}$ disturbs the spectral analysis of the redox state of *Bs*FNR in this procedure (Fig. S2b), the spectral changes in the 400–500 nm and 550–670 nm regions give us information about the amount of $Bs\text{FNR}_{ox}$ and $Bs\text{FNR}_{sq}$ (Fig. S2c). The small peak at approximately 380 nm and the peak/shoulder at about 460 nm in the spectrum at 0 ms in Figure 4a indicate the presence of a small amount of $Bs\text{FNR}_{ox}$. These features rapidly disappeared with time. The appearance of the absorption bands at approximately 650 nm in the spectrum at 0 ms indicates the formation of a neutral semiquinone state, which gradually decreased with time. The corresponding oxidation of $Bs\text{Fd}_{red}$ was demonstrated by the increase in absorbance in the 700–800 nm region (Figs. 4a and S2b) [39]. After 500 ms, the spectra did not significantly change (data not shown). As shown in Figures 4a and S2a, the magnitudes of the absorption bands corresponding to $Bs\text{FNR}_{ox}$ and $Bs\text{FNR}_{sq}$ were very small at 499 ms (Figs. 4a, S2b, c), thereby indicating that most of the $Bs\text{FNR}_{ox}$ was reduced to a hydroquinone state at equilibrium.

By subtracting the spectrum at 0 ms from the spectra at the indicated times, we estimated the redox transitions of *Bs*FNR and *Bs*Fd (Fig. 4b). The transition corresponded to the differences in the absorption spectra of [$<Bs\text{FNR}_{ox} - Bs\text{FNR}_{sq}> + <Bs\text{Fd}_{red} - Bs\text{Fd}_{ox}>$], [$<Bs\text{FNR}_{ox} - Bs\text{FNR}_{red}> + 2\times<Bs\text{Fd}_{red} - Bs\text{Fd}_{ox}>$] and [$<Bs\text{FNR}_{sq} - Bs\text{FNR}_{red}> + <Bs\text{Fd}_{red} - Bs\text{Fd}_{ox}>$] represented in Figure S2d,. These were estimated based on the difference spectra of $Bs\text{Fd}_{red}$ minus $Bs\text{Fd}_{ox}$ and $Bs\text{FNR}_{sq}$ minus $Bs\text{FNR}_{red}$ (Fig. S2b and c, respectively), without taking into consideration the spectral

perturbations caused by complex formations. In the transient spectra, the reduction of *Bs*FNR$_{sq}$ to *Bs*FNR$_{red}$ and the accumulation of *Bs*Fd$_{ox}$ were identified as shown by the decreases in the absorption bands with peaks at 600 and 650 nm and the increases at 415 and 700 nm, respectively (Fig. 4b, S2d). The transient difference spectra induced by mixing *Bs*FNR$_{ox}$ with 40–120 μM *Bs*Fd$_{red}$ had essentially the same spectral profile. A_{600} minus A_{685} (for correction of signal drift) in the transient difference spectra can be approximated to a single step reaction model (Fig. 4c) as the reduction of *Bs*FNR kinetically coupled with the oxidation of *Bs*Fd, and most of *Bs*FNR was reduced to *Bs*FNR$_{sq}$ after 2 ms (Fig. 4a). The deduced rate significantly increased as the *Bs*Fd$_{red}$ concentration increased (inset of Fig. 4c).

To study the effects of low concentrations of *Bs*Fd$_{ox}$ on the kinetics of the *Bs*FNR reduction by *Bs*Fd$_{red}$, which should occur during the reduction of *Bs*FNR$_{sq}$ by *Bs*Fd$_{red}$, 12 μM *Bs*FNR$_{ox}$, which had been pre-incubated with *Bs*Fd$_{ox}$ (15 μM) beforehand, was rapidly mixed with *Bs*Fd$_{red}$ (100 μM), and the spectral change was followed (Fig. 4d). In contrast to the spectra obtained in the absence of premixing with *Bs*Fd$_{ox}$ (Fig. 4b), the reduction of *Bs*FNR$_{ox}$ to *Bs*FNR$_{red}$ by *Bs*Fd$_{red}$ was visualized as a trough at about 480 nm (Figs. 4d, S2d), together with a smaller signal corresponding to the transition from *Bs*FNR$_{sq}$ to *Bs*FNR$_{red}$ in the 600–650 nm region (Fig. 4b). This indicated that the rate of reduction of *Bs*FNR$_{ox}$ by the first *Bs*Fd$_{red}$ had been dramatically decreased because of prior binding with *Bs*Fd$_{ox}$.

4. Discussion

4.1.1 Formation of CTCs with $NADP^+$/NADPH

Previous steady-state studies of the spectral changes in *Bs*FNR caused by mixing with sodium dithionite, $NADP^+$ or NADPH [21, 43] resulted in several changes in the spectrum. One, when *Bs*FNR_{ox} was reduced with dithionite, the magnitude of the absorbance significantly decreased in the 400–500 nm region and a smaller absorption band appeared at approximately 430 nm similar to the photochemically reduced spectrum shown in Figure 3a. The addition of $NADP^+$ to *Bs*FNR_{ox} induced major changes in the absorbance in the 300–550 nm region, whereas almost no changes were observed in the 550–600 nm region [21, 43]. Thirdly, when excess amounts of NADPH were mixed with *Bs*FNR_{ox}, the magnitude of the absorbance in the 400–500 nm region decreased and yielded a smaller absorption band with a maximum at approximately 450 nm and a discernible gentle slope extending to 700 nm [21]. The difference spectrum of [*Bs*FNR-NADPH] minus [dithionite-reduced *Bs*FNR] had positive broad bands from 520–700 nm with peaks in the 550–650 nm region. These bands appeared only in the presence of NADPH, and were ascribed to the formation of either one or both of CTC-1 (NADPH-FNR_{ox}) and CTC-2 ($NADP^+$-FNR_{red}) (Scheme 1) [21]. In the present study, the transient spectra observed during the pre-steady-state reactions of *Bs*FNR_{ox} with NADPH and *Bs*FNR_{red} with $NADP^+$ showed that the redox reaction involved the rapid formation of CTCs with a shoulder/peak in the 550–620 nm region and a discernible slope extending to 700 nm. However, in the previous study, the spectrum of *Bs*FNR observed after mixing with an excess amount of NADPH contained small additional absorption bands with peaks at 600 and 650 nm [21]. In the present study, the latter peak was not observed in the transient spectra (Figs. 1a, 3b and 3c), and the absorption bands observed in the previous study were similar to those of the semiquinone form in the present studies (Figs. 3a and S2c). Thus, the previously reported spectra in [21] arose from contamination by neutral semiquinone in a small amount, which possibly occurred via electron escape to contaminated O_2 because of incomplete anaerobiosis.

Plastid-type FNRs and *Ec*TrxR generally show two broad absorption bands over 500 nm, one with a peak at approximately 600 nm and the other with a peak at about 700 nm, which are generally assigned to the formation of CTC-1 and CTC-2, respectively [27, 28, 58, 59]. In the case of plant-type *An*FNR and *Ec*TrxR, the transition from

CTC-1 to CTC-2 induces a noticeable red shift in the CT absorption band by more than 50 nm [27, 28, 60]. For *Bs*FNR, the absorption band of CTC-1 at 600 nm did not differ greatly from that of CTC-2 in shape although on closer examination, a slight shift of the peak to a longer wavelength was noted in CTC-2 compared with CTC-1 (Figs. 1a, 2a, 3b and 3c). In contrast to the other FNRs and *Ec*TrxR, *Bs*FNR's CTC-2 did not have a discernible absorption band with a peak beyond 650 nm. The molar absorption coefficient of CTC-2 in the CT band region seems to be smaller than CTC-1 from comparison of the spectra at 0 ms in Figure 1a and Figure 3b. The fact that the absorbance in the CT band region decreased with a roughly comparable time constant in the flavin absorption band I region during the *Bs*FNR_{ox} reduction reaction by NADPH and NADPD (Figs. 1a, 2a, 2c) also suggests a smaller absorption coefficient for CTC-2 than CTC-1 in the CT band region. However, according to Scheme 1, if the value of k_4 is much larger than k_3 and MC-2 is dominant at equilibrium over CTC-2 ($k_4 > k_{-4}$), a CT absorption coefficient for CTC-2 comparable with that of CTC-1 can result in similar absorption changes. The equilibrium between MC-1 and CTC-1, and MC-2 and CTC-2 occurred very rapidly (Figs. 2c, 3c, 3d). Therefore, we could not kinetically distinguish MC-1 and CTC-1, and MC-2 and CTC-2, and we could not conclude whether the absorption coefficient of CT band of CTC-2 is smaller than that of CTC-1 or not.

4.1.2 Kinetics of the reaction between BsFNR and $NADP^+$/NADPH

In the *Bs*FNR_{ox} reduction reaction with NADPH, the initial phase of increase in absorbance in the CT band region (A_{590}) was almost complete within 1 ms (Fig. 1a). This implies that the rate constants for the association with NADPH (k_1 in Scheme 1) and the transition from MC-1 to CTC-1 (k_2 in Scheme 1) are larger than 3×10^7 $M^{-1}s^{-1}$ and 5,000 s^{-1}, respectively (Fig. S3a and b). The fact that the rise in initial CT band intensity showed almost no dependency of NADPH concentration in 100–500 μM range in the *Bs*FNR_{ox} reduction with NADPH also indicates that the initial association is strong. In the *Bs*FNR_{red} oxidation reaction with $NADP^+$, A_{590} rapidly increased, and its intensity was almost independent of the $NADP^+$ concentration in the 100–500 μM range (inset in Fig. 3c), indicating that CTC-2 formation occurred rapidly. Thus, the rate-limiting step under the experimental conditions is the hydride-transfer process between CTC-1 and CTC-2 in both directions.

The apparent rate of *Bs*FNR$_{ox}$ reduction by NADPH (Fig. 1b) was much faster than that of the *Bs*FNR$_{red}$ oxidation reaction by NADP$^+$ (Fig. 3d), and was almost independent of NADPH concentration in the 100–500 μM range. Therefore, we estimated an apparent rate of 500 s^{-1} for *Bs*FNR$_{ox}$ reduction by NADPH (Fig. 1b) for k_3 in Scheme 1. The fitted curve against ε_{458} with NADPH and NADPD have an intersection point at approximately 0 ms (Fig. 2b inset), indicating both curves traced the same transition phase. Both curves provide a significant drop in ε_{458} at 0 ms against ε_{458} of *Bs*FNR$_{ox}$ (12 mM^{-1}cm^{-1}, [17]), indicating there is another rapid phase related to the formation of either MC-1 or CTC-1 or both.

In the *Bs*FNR$_{red}$ oxidation reaction with NADP$^+$, A_{458} continued to slowly rise from 0 to 1000 ms in an NADP$^+$ concentration-dependent manner (Fig. 3d), and the observed rate decreased as the NADP$^+$ concentration increased (Fig. 3e). Therefore, k_{-3} could not be directly estimated from the observed data because either an increase in the value of k_{-3} or a decrease in the value of k_{-2} (model 1, 4–5 in Table S1) could lead to similar NADP$^+$ concentration-dependent accumulations of oxidized *Bs*FNR (Fig. S3c). However, an increase in the value of k_{-3} would result in an increase in the amount of the pre-steady-state rapid phase ($k_{obs} \approx k_3 + k_{-3}$) observed in the change of A_{458} in the reverse direction because the Δabsorbance of this phase responds to the ratio of $k_{-3}/(k_3 + k_{-3})$ (Fig. S3c). The results shown in Figure 3d indicate that the rapid phase was too small to be observed indicating that k_{-3} was estimated to be less than 10 s^{-1} (Figs. 3d and S3c).

Scheme 1 is a minimal depiction of the reaction that only contains one NADP$^+$ concentration-dependent process before the rate-limiting hydride transfer process has occurred. To explain the dependency of the observed rates of A_{458} on the NADP$^+$ concentration in Figure 3d, an additional NADP$^+$ concentration-dependent reaction step(s) is needed after the rate-limiting hydride transfer process. The dependencies of the change in absorbance on the NADP$^+$

$$FNR_{ox} + NADP^+ \underset{k_{-6}}{\overset{k_{+6}}{\rightleftharpoons}} FNR_{ox}\_NADP$$

Scheme 2

concentration (Fig. 3d) can be explained by assuming that the interaction between NADP$^+$ and FNR$_{ox}$ formed a NADP$^+$-FNR$_{ox}$ non-productive complex as previously described [28, 30, 61, 62] (Scheme 2). This complex will trap FNR$_{ox}$ and increase the amount of FNRs$_{ox}$ as the NADP$^+$ concentration increases, thereby leading to an increase in

the change in the total absorbance and a decrease in the observed rate constant (Fig. 3d, e). The $NADP^+$ concentration-dependent changes in the absorbance during the *Bs*FNR_{red} oxidation reaction with $NADP^+$, as shown in Figure 3d, could be explained by the formation of the *Bs*FNR_{ox}–$NADP^+$ complex as shown by the simulations (Fig. S3d and e).

*Bs*FNR is a homodimeric protein where each protomer contains one FAD prosthetic group [23]. In this paper, we assumed that each FAD in the different protomers of the same molecule behaves in exactly the same way under the experimental conditions because we observed no evidence for the presence of two kinetically different components. The validity of this assumption is open to further examination. In the homodimer flavoprotein *Ec*TrxR, no difference in kinetic behaviors between protomers has been reported [30].

4.2 BsFNR reduction by reduced BsFd

The transient spectra obtained after mixing *Bs*FNR_{ox} with *Bs*Fd_{red} showed that the reduction of *Bs*FNR_{ox} by the first *Bs*Fd_{red} was so rapid that it was difficult to follow the transition with our stopped-flow equipment, whereas the second reduction rate was much slower and traceable. Based on the generally accepted kinetic processes for the reaction between Fd and FNR as shown in Schemes 3–5 [2, 28], the absorption changes corresponding to FNR reduction from the oxidized state to the semiquinone state involve two elementary reactions, that is, the association of Fd_{red} to FNR_{ox} and an internal electron transfer in the transient Fd_{red}–FNR_{ox} complex (Scheme 3) [2, 28]. The

$$FNR_{ox} + Fd_{red} \underset{k_{-7}}{\overset{k_{+7}}{\rightleftharpoons}} FNR_{ox}Fd_{red} \underset{k_{-8}}{\overset{k_{+8}}{\rightleftharpoons}} FNR_{sq}Fd_{ox} \underset{k_{-9}}{\overset{k_{+9}}{\rightleftharpoons}} FNR_{sq} + Fd_{ox}$$

Scheme 3

$$FNR_{sq} + Fd_{red} \underset{k_{-10}}{\overset{k_{+10}}{\rightleftharpoons}} FNR_{sq}Fd_{red} \underset{k_{-11}}{\overset{k_{+11}}{\rightleftharpoons}} FNR_{hq}Fd_{ox} \underset{k_{-12}}{\overset{k_{+12}}{\rightleftharpoons}} FNR_{hq} + Fd_{ox}$$

Scheme 4

$$FNR_{ox} + Fd_{ox} \underset{k_{-13}}{\overset{k_{+13}}{\rightleftharpoons}} FNR_{ox}Fd_{ox}$$

Scheme 5

majority of these two elementary reactions were complete within a few milliseconds (Fig. 4a). Based on $\Delta(A_{600}$ - $A_{600})$ (Figs. 4a and S2c), we can assume that more than 75% of *Bs*FNR_{ox} was reduced to *Bs*FNR_{sq} within 1 ms in the presence of 40 μM *Bs*Fd_{red}. This implies that the rate constants for the association of *Bs*Fd_{red} and the subsequent

electron transfer process were larger than 3×10^7 M^{-1} s^{-1} and 1,500 s^{-1} ($e^{-k \times 0.001} < 0.25$), respectively, which are comparable with those of plant-type FNRs and PdRs [28, 32, 34, 38].

The transition from FNR_{sq} to FNR_{red} involves the following consecutive elementary reactions: dissociation of the first Fd_{ox}, association of a second Fd_{red}, and internal electron transfer in the transient Fd_{red}–FNR_{sq} complex (Schemes 3 and 4) [2, 28]. If we assume that the association of *Bs*Fd_{red} with *Bs*FNR_{ox} is kinetically comparable with that of *Bs*FNR_{sq}, then the rate-determining step is either the dissociation of the first *Bs*Fd_{ox} or the internal electron transfer. If the rate-limiting step is electron transfer in the transient *Bs*FNR_{sq}–*Bs*Fd_{red} complex, then a substantial amount of *Bs*FNR_{sq} would remain at equilibrium, which contradicts our observations because the rate of the reverse direction of this step (k_{-11}) should be larger than the rate of the cytochrome *c* reduction assay (~50 s^{-1} at 25°C) [43].

The direction of the above reaction is opposite to the physiological one. From the redox equilibrium in Figure 4a and c, the k_{-8} and k_{-11} values were estimated to be much smaller than those of k_8 and k_{11}. Thus, the k_{-8} and k_{-11} values would be close to the turnover rate observed in the steady-state assay in the physiological direction (~50 s^{-1}) [43]. Similar kinetic behavior has been reported in the plastid-type FNR system [28], where the dissociation process of Fd_{ox} (Schemes 3 and 4) was considered to be the rate-limiting step [2, 28]. For AdR, internal electron transfer between AdR-bound dimeric Ad molecules has been proposed [3], but this process does not seem to significantly contribute to the overall reaction with *Bs*FNR because electron transfer is slow between the *Bs*FNR_{ox}–*Bs*Fd_{ox} complex and free *Bs*Fd_{red} (Fig. 4d). A recent study of a *Tt*Fd–*Tt*FNR fusion protein indicated that the addition of extra *Tt*Fd did not enhance the reduction rate [63].

In this study, based on investigations of the pre-steady-state kinetics using stopped-flow spectrophotometry, we determined the kinetics of some of the elementary steps in the reactions between *Bs*FNR and $NADP^+$/NADPH, as well as *Bs*FNR and *Bs*Fd. The reactions of *Bs*FNR with $NADP^+$ and NADPH yielded two types of CTCs with typical broad CT absorption bands centered at approximately 600 nm. In the overall reaction, the rate-determining step in both directions was the hydride transfer, where the forward direction rate was much faster than the reverse direction rate. The reaction of reduced *Bs*Fd (*Bs*Fd_{red}) with *Bs*FNR_{ox} induced rapid formation of a neutral semiquinone radical within the instrument's dead time (~1 ms). The subsequent reduction of a neutral semiquinone radical to

hydroquinone is slower, where the dissociation of oxidized Fd from *Bs*FNR$_{sq}$ is rate-limiting. In the present study, no substrate inhibition was observed in the reaction with either $NADP^+$, NADPH or *Bs*Fd.

Acknowledgement

DS thanks the Japanese Ministry of Education, Culture, Sports, Science and Technology for an international exchange fellowship.

References

[1] D.B. Knaff, M. Hirasawa, Ferredoxin-dependent chloroplast enzymes, Biochim. Biophys. Acta 1056 (1991) 93-125.

[2] N. Carrillo, E.A. Ceccarelli, Open questions in ferredoxin-$NADP^+$ reductase catalytic mechanism, Eur. J. Biochem. (2003) 1900-1915.

[3] K.M. Ewen, M. Kleser, R. Bernhardt, Adrenodoxin: The archetype of vertebrate-type [2Fe-2S] cluster ferredoxins, Biochim. Biophys. Acta 1814 (2011) 111-125.

[4] J.T. Wan, J.T. Jarrett, Electron acceptor specificity of ferredoxin (flavodoxin):$NADP^+$ oxidoreductase from *Escherichia coli*, Arch. Biochem. Biophys. 406 (2002) 116-126.

[5] A.W. Munro, H.M. Girvan, K.J. McLean, Cytochrome P450-redox partner fusion enzymes, Biochim. Biophys. Acta 1770 (2007) 345-359.

[6] A. Marquet, B. Tse Sum Bui, A.G. Smith, M.J. Warren, Iron-sulfur proteins as initiators of radical chemistry, Nat. Prod. Rep. 24 (2007) 1027-1040.

[7] V. Bianchi, P. Reichard, R. Eliasson, E. Pontis, M. Krook, H. Jornvall, E. Haggard- Ljungquist, *Escherichia coli* ferredoxin $NADP^+$ reductase: Activation of *E. coli* anaerobic ribonucleotide reduction, cloning of the gene (*fpr*), and overexpression of the protein, J. Bacteriol. 175 (1993) 1590-1595.

[8] J.W. Chu, T. Kimura, Studies on adrenal steroid hydroxylases. Molecular and catalytic properties of adrenodoxin

reductase (a flavoprotein), J. Biol. Chem. 248 (1973) 2089-2094.

[9] T. Omura, E. Sanders, R.W. Estabrook, D.Y. Cooper, O. Rosenthal, Isolation from adrenal cortex of a nonheme iron protein and a flavoprotein functional as a reduced triphosphopyridine nucleotide-cytochrome P-450 reductase, Arch. Biochem. Biophys. 117 (1966) 660-673.

[10] M. Katagiri, B.N. Ganguli, I.C. Gunsalus, A soluble cytochrome P-450 functional in methylene hydroxylation, J. Biol. Chem. 243 (1968) 3543-3546.

[11] F. Xu, S.G. Bell, Y. Peng, E.O.D. Johnson, M. Bartlam, Z. Rao, L.-L. Wong, Crystal structure of a ferredoxin reductase for the CYP199A2 system from *Rhodopseudomonas palustris,* Proteins 77 (2009) 867-880.

[12] T. Senda, T. Yamada, N. Sakurai, M. Kubota, T. Nishizaki, E. Masai, M. Fukuda, Y. Mitsui, Crystal structure of NADH-dependent ferredoxin reductase component in biphenyl dioxygenase, J. Mol. Biol. 304 (2000) 397-410.

[13] A. Aliverti, V. Pandini, A. Pennati, M. de Rosa, G. Zanetti, Structural and functional diversity of ferredoxin-$NADP^+$ reductases, Arch. Biochem. Biophys. 474 (2008) 283-291.

[14] E.A. Ceccarelli, A.K. Arakaki, N. Cortez, N. Carrillo, Functional plasticity and catalytic efficiency in plant and bacterial ferredoxin-NADP(H) reductases, Biochim. Biophys. Acta 1698 (2004) 155-165.

[15] O. Dym, D. Eisenberg, Sequence-structure analysis of FAD-containing proteins, Protein Sci. 10 (2001) 1712-1728.

[16] C.C. Correll, M.L. Ludwig, C.M. Bruns, P.A. Karplus, Structural prototypes for an extended family of

flavoprotein reductases: comparison of phthalate dioxygenase reductase with ferredoxin reductase and ferredoxin, Protein Sci. 2 (1993) 2112-2133.

[17] D. Seo, K. Kamino, K. Inoue, H. Sakurai, Purification and characterization of ferredoxin-$NADP^+$ reductase encoded by *Bacillus subtilis yumC*, Arch. Microbiol. 18
2 (2004) 80-89.

[18] T. Mandai, S. Fujiwara, S. Imaoka, A novel electron transport system for thermostable CYP175A1 from *Thermus thermophilus* HB27, FEBS J. 276 (2009) 2416-2429.

[19] N. Muraki, D. Seo, T. Shiba, T. Sakurai, G. Kurisu, Asymmetric dimeric structure of ferredoxin-$NAD(P)^+$ oxidoreductase from the green sulfur bacterium *Chlorobaculum tepidum*: Implications for binding ferredoxin and $NADP^+$, J. Mol. Biol. 401 (2010) 403-414.

[20] D. Seo, H. Sakurai, Purification and characterization of ferredoxin-$NADP^+$ reductase from the green sulfur bacterium *Chlorobium tepidum*, Biochim. Biophys. Acta 1597 (2002)123-132.

[21] D. Seo, S. Okabe, M. Yanase, K. Kataoka, T. Sakurai, Studies of interaction of homo-dimeric ferredoxin-$NAD(P)^+$ oxidoreductases of *Bacillus subtilis* and *Rhodopseudomonas palustris*, that are closely related to thioredoxin reductases in amino acid sequence, with ferredoxins and pyridine nucleotide coenzymes, Biochim. Biophys. Acta 1794 (2009) 594-601.

[22] Z. Yan, Y.-W. Nam, S. Fushinobu, T. Wakagi, *Sulfolobus tokodaii* ST2133 is characterized as a thioredoxin reductase-like ferredoxin:$NADP^+$ oxidoreductase, Extremophiles 18 (2014) 99-110.

[23] H. Komori, D. Seo, T. Sakurai, Y. Higuchi, Crystal structure analysis of *Bacillus subtilis* ferredoxin-$NADP^+$ oxidoreductase and the structural basis for its substrate selectivity, Protein Sci. 19 (2010) 2279-2290.

[24] C.H. Williams Jr., L. David Arscott, S. Müller, B.W. Lennon, M.L. Ludwig, P.-F Wang, D.M. Veine, K. Becker, R. Heiner Schirmer, Thioredoxin reductase: Two modes of catalysis have evolved,
Eur. J. Biochem. 267 (2000) 6110-6117.

[25] G. Waksman, T.S.R. Krishna, C.H. Williams Jr., J. Kuriyan, Crystal structure of *Escherichia coli* thioredoxin reductase refined at 2 Å resolution: Implications for a large conformational change during catalysis, J. Mol. Biol. 236 (1994) 800-816.

[26] V. Massey, R.G. Matthews, G.P. Foust, L.G. Howell, C.H. Williams Jr., G. Zanetti, S. Ronchi, A new intermediate in TPNH-linked flavoproteins, in H. Sund (Eds.), Pyridine Nucleotide-dependent Dehydrogenases, Springer-Verlag, Berlin, 1970, pp. 393-411.

[27] J. Tejero, JR. Peregrina, M. Martínez-Júlvez, A. Gutiérrez, C. Gómez-Moreno, NS. Scrutton, M. Medina, Catalytic mechanism of hydride transfer between $NADP^+$/H and ferredoxin-$NADP^+$ reductase from *Anabaena* PCC 7119, Arch. Biochem. Biophys. 459 (2007) 79-90.

[28] C.J. Batie, H. Kamin, Electron transfer by ferredoxin:$NADP^+$ reductase. Rapid-reaction evidence for participation of a ternary complex, J. Biol. Chem. 259 (1984) 11976-11985.

[29] K.J. McLean, N.S. Scrutton, A.W. Munro, Kinetic, spectroscopic and thermodynamic characterization of the *Mycobacterium tuberculosis* adrenodoxin reductase homologue FprA, Biochem. J. 372 (2003) 317-327.

[30] B.W. Lennon, C.H. Williams Jr., Reductive half-reaction of thioredoxin reductase from *Escherichia coli,* Biochem. 36 (1997) 9464-9477.

[31] J.D. Lambeth, H. Kamin, Adrenodoxin reductase and adrenodoxin. Mechanisms of reduction of ferricyanide and cytochrome *c*. J. Biol Chem. 252 (1977) 2908-2917.

[32] V.Y. Kuznetsov, E. Blair, P.J. Farmer, T.L. Poulos, A. Pifferitti, I.F. Sevrioukova, The putidaredoxin reductase-putidaredoxin electron transfer complex: theoretical and experimental studies, J. Biol Chem. 280 (2005) 16135-16142.

[33] P.W. Roome, J.A. Peterson, The oxidation of reduced putidaredoxin reductase by oxidized putidaredoxin, Arch. Biochem. Biophys. 266 (1988) 41-50.

[34] N. Cassan, B. Lagoutte, P. Sétif, Ferredoxin-$NADP^+$ reductase. Kinetics of electron transfer, transient intermediates, and catalytic activities studied by flash-absorption spectroscopy with isolated photosystem I and ferredoxin, J. Biol Chem. 280 (2005) 25960-25972.

[35] C. Gómez-Moreno, M. Martínez-Júlvez, M. Medina, J.K. Hurley, G. Tollin, Protein-protein interaction in electron transfer reactions: the ferredoxin/flavodoxin/ferredoxin:$NADP^+$ reductase system from *Anabaena*, Biochimie 80 (1998) 837-846.

[36] M. Martínez-Júlvez, M. Medina, J.K. Hurley, R. Hafezi, T.B. Brodie, G. Tollin, C. Gómez-Moreno, Lys75 of *Anabaena* ferredoxin-$NADP^+$ reductase is a critical residue for binding ferredoxin and flavodoxin during electron transfer, Biochem. 37 (1998) 13604-13613.

[37] J.K. Hurley, M.F. Fillat, C. Gémez-Moreno, G. Tollin, Electrostatic and hydrophobic interactions during complex

formation and electron transfer in the ferredoxin/ferredoxin:$NADP^+$ reductase system from Anabaena, J. Am. Chem. Soc. 118 (1996) 5526-5531.

[38] J.K. Hurley, R. Morales, M. Martínez-Júlvez, T.B. Brodie, M. Medina, C. Gómez-Moreno, G. Tollin, Structure-function relationships in Anabaena ferredoxin/ferredoxin:$NADP^+$ reductase electron transfer: Insights from site-directed mutagenesis, transient absorption spectroscopy and X-ray crystallography, Biochim. Biophys. Acta 1554 (2002) 5-21.

[39] A.J. Green, A.W. Munro, M.R. Cheesman, G.A. Reid, C. Von Wachenfeldt, S.K. Chapman, Expression, purification and characterisation of a *Bacillus subtilis* ferredoxin: A potential electron transfer donor to cytochrome P450 BioI, J. Inor. Biochem. 93 (2003) 92-99.

[40] Z.-Q. Wang, R.J. Lawson, M.R. Buddha, C.-C. Wei, B.R. Crane, A.W. Munro, D.J. Stuehr, Bacterial flavodoxins support nitric oxide production by *Bacillus subtilis* nitric-oxide synthase, J. Biol. Chem. 282 (2007) 2196-2202.

[41] L. Chazarreta-Cifre, L. Martiarena, D. de Mendoza, S.G. Altabe, Role of ferredoxin and flavodoxins in *Bacillus subtilis* fatty acid desaturation, J. Bacteriol. 193 (2011) 4043-4048.

[42] J.K. Holden, N. Lim, T.L. Poulos, Identification of redox partners and development of a novel chimeric bacterial nitric oxide synthase for structure activity analyses, J. Biol. Chem. 289 (2014) 29437-29445.

[43] D. Seo, T. Asano, H. Komori, T. Sakurai, Role of the C-terminal extension stacked on the *re*-face of the isoalloxazine ring moiety of the flavin adenine dinucleotide prosthetic group in ferredoxin-$NADP^+$ oxidoreductase from *Bacillus subtilis*, Plant Phys. Biochem. 81 (2014) 143-148.

[44] H. Roder, K. Maki, H. Cheng, M.C. Ramachandra Shastry, Rapid mixing methods for exploring the kinetics of protein folding, Methods 34 (2004) 15-27.

[45] B. Tonomura, H. Nakatani, M. Ohnishi, J. Yamaguchi-Ito, K. Hiromi, Test reactions for a stopped-flow apparatus. Reduction of 2,6 dichlorophenolindophenol and potassium ferricyanide by L-ascorbic acid, Anal. Biochem. 84 (1978) 370-383.

[46] G. Zanetti, B. Curti, Interactions between ferredoxin-$NADP^+$ reductase and ferredoxin at different reduction levels of the two proteins, FEBS Lett. 129 (1981) 201-204.

[47] C.G. Bowsher, L.M. Eyres, J.O. Gummadova, P. Hothi, K.J. McLean, A.W. Munro, N.S. Scrutton, G.T. Hanke, Y. Sakakibara, T. Hase, Identification of N-terminal regions of wheat leaf ferredoxin $NADP^+$ oxidoreductase important for interactions with ferredoxin, Biochem. 50 (2011) 1778-1787.

[48] E.E. Carlson, L.L. Kiessling, Improved chemical syntheses of 1- and 5-deazariboflavin, J. Org. Chem. 69 (2004) 2614-2617.

[49] C. Walsh, J. Fisher, R. Spencer, D.W. Graham, W.T. Ashton, J.E. Brown, R.D. Brown, E.F. Rogers, Chemical and enzymatic properties of riboflavin analogues, Biochem. 17 (1978) 1942-1951.

[50] S. Hoops, S. Sahle, R. Gauges, C. Lee, J. Pahle, N. Simus, M. Singhal, L. Xu, P. Mendes, U. Kummer, COPASI — a COmplex PAthway Simulator, Bioinform. 22 (2006) 3067-3074.

[51] Viola, R.E., Cook, P.F., Cleland, W.W., Stereoselective preparation of deuterated reduced nicotinamide adenine nucleotides and substrates by enzymatic synthesis

Anal. Biochem. 96 (1979) 334-340.

[52] G. Ottolina, S. Riva, G. Carrea, B. Danieli, AF. Buckmann, Enzymatic synthesis of [4*R*-^{2}H]NAD(P)H and [4*S*-^{2}H]NAD(P)H and determination of the stereospecificity of 7α- and 12α-hydroxysteroid dehydrogenase, Biochim. Biophys. Acta 998 (1989) 173-178.

[53] V.V. Pollock, M.J. Barber, Kinetic and mechanistic properties of biotin sulfoxide reductase, Biochemistry 40 (2001) 1430-1440.

[54] R.N. Ammeraal, G. Krakow, B. Vennesland, The Stereospecificity of the Hill reaction with diphosphopyridine, J. Biol. Chem. 240 (1965) 1824-1828.

[55] C.J. Sih, Y.Y. Tsong, B. Stein, The roles of reduced nicotinamide-adenine dinucleotide phosphate in steroid hydroxylation, J. Am. Chem. Soc., 90 (1968) 5300-5302.

[56] D.R. Light, C. Walsh, Flavin analogs as mechanistic probes of adrenodoxin reductase-dependent electron transfer to the cholesterol side chain cleavage cytochrome P-450 of the adrenal cortex, J. Biol. Chem. 255 (1980) 4264-4277.

[57] K.S. You, Stereospecificity for nicotinamide nucleotides in enzymatic and chemical hydride,
CRC Crit. Rev. Biochm, 17 (1985) 313-451.

[58] B.W. Lennon, C.H. Williams Jr., Enzyme-monitored turnover of *Escherichia coli* thioredoxin reductase: Insights for catalysis, Biochemistry 35 (1996) 4704-4712.

[59] G. Blankenhorn, Flavin nicotinamide biscoenzymes: models for the interaction between NADH (NADPH) and

flavin in flavoenzymes. Reaction rates and physicochemical properties of intermediate species, Eur. J. Biochem. 50 (1975) 351-356.

[60] A. Bortolotti, I. Pérez-Dorado, G. Goñi, M. Medina, J.A. Hermoso, N. Carrillo, N. Cortez, Coenzyme binding and hydride transfer in *Rhodobacter capsulatus* ferredoxin/flavodoxin NADP(H) oxidoreductase, Biochim. Biophys. Acta 1794 (2009) 199-210.

[61] S. Daff, An Appraisal of multiple NADPH binding-site models proposed for cytochrome P450 reductase, NO synthase, and Diflavin Reductase System, Biochem. 43 (2004) 3929-3932.

[62] C.J. Batie, H. Kamin, Association of ferredoxin-$NADP^+$ reductase with NADP(H) specificity and oxidation-reduction properties, J. Biol. Chem. 261 (1986) 11214-11223.

[63] T. Mandai, S. Fujiwara, S. Imaoka, Construction and engineering of a thermostable self-sufficient cytochrome P450, Biochem. Biophys. Res. Com. 384 (2009) 61-65.

Figure 1. (**a**) Transient spectra induced by mixing 12 μM *Bs*FNR with 100 μM NADPH. The reaction was performed in 20 mM HEPES-NaOH buffer (pH 7.0) at 10°C. The spectrum at 0 ms is shown as a thin continuous line with × marks. The spectra shown by thin dotted lines from the top to the bottom at 450 nm correspond to those at 1, 2, 4, 6, 9, 19, 49 and 99 ms. The spectrum of *Bs*FNR$_{ox}$ was obtained by mixing 12 μM *Bs*FNR$_{ox}$ with 20 mM HEPES-NaOH buffer (pH 7.0) in the absence of NADPH (thick continuous line). The spectrum of *Bs*FNR$_{red}$ obtained by photochemical reduction, as described in Figure 2a, is shown as a thick continuous line for reference. The arrows indicate the directions of the changes in absorbance at the respective wavelengths, where the dotted part indicates that the change occurred within the first acquisition period (1 ms). The inset shows the time course of A_{590} at 100 μM NADPH (●) and 500 μM NADPH (□), respectively. (**b**) The time course of A_{458} after mixing *Bs*FNR$_{ox}$ with NADPH. The measurement conditions were the same as those in Figure 1a, except the NADPH concentrations were as follows: 0 (○), 100 (●), 200 (■) and 500 μM (▲). The data are an average of four to five measurements. The time course in the short time range is shown in the inset. Single exponential decay curves based on the data for each NADPH concentration are indicated by continuous lines in the inset.

Figure 2. (**a**) Transient spectra induced by mixing 10 μM *Bs*FNR with 100 μM NADPD. The reaction was performed in 20 mM HEPES-NaOH buffer (pH 7.0) at 10°C. The spectrum at 0 ms is shown by the thin continuous line with × marks. The spectra shown by thin dotted lines from the top to the bottom at 450 nm correspond to those at 2, 4, 6, 9, 14, 19, 49 and 99 ms. The spectrum of *Bs*FNR$_{ox}$ in 20 mM HEPES-NaOH buffer (pH 7.0) was represented by the thick continuous line. The arrows indicate the directions of the changes in absorbance at the respective wavelengths, where the dotted part indicates that the change occurred within the first acquisition period (1 ms). The inset shows the time course of A_{590} at 100 μM NADPD (●) and 500 μM NADPD (□), respectively. (**b**) The time course of A_{458} after mixing *Bs*FNR$_{ox}$ with NADPD. The measurement conditions were the same as those in Figure 2a, except the NADPD concentrations were as follows: 0 (○), 100 (●), 200 (×) and 500 μM (▲). The data are the average of four measurements. The fitted single exponential decay curves based on the data for each NADPD concentration are indicated by continuous lines. Inset: time course of ε_{458} in the reactions where *Bs*FNR$_{ox}$ was mixed with 100 μM

NADPH (○) and 100 μM NADPD (□) as described in Figure 1a and 2a, respectively. The absorbance was normalized by *Bs*FNR concentration. (**c**) The relationship of $-\Delta\varepsilon_{458}$ and ε_{590} in the reaction of *Bs*FNR$_{ox}$ with 100 μM NADPH (Δ) and 100 μM NADPD (○). The data were obtained from Fig. 1a (NADPH) and Fig. 2a (NADPD) and normalized by the *Bs*FNR concentrations. The $-\Delta\varepsilon_{458}$ was estimated by assuming ε_{458} = 10.0 $mM^{-1}cm^{-1}$ for MC-1/CTC-1 (inset of Fig. 2a) and subtracting the ε_{458} of *Bs*FNR$_{red}$ (2.7 $mM^{-1}cm^{-1}$). The arrows indicate the direction of the time course while the dashed arrows indicate that the change occurred within the first acquisition period (1 ms). The dotted line represents the respective CTC-1 content.

Figure 3. (**a**) The spectral changes induced by the photochemical reduction of *Bs*FNR$_{ox}$. *Bs*FNR$_{ox}$ (40 μM) in 20 mM HEPES-NaOH buffer (pH 7.0) containing 1.2 μM dRf and 2 mM EDTA was irradiated using a 150 W xenon discharge lamp through a light guide under anaerobic conditions. The spectra are shown after successive illumination for 0, 30, 60, 90, 120, 150, 240, 360 and 480 s. The spectra after 0 and 480 s are shown by thick and thin continuous lines, respectively. The spectrum at 90 s is shown by a thin continuous line with × marks, whereas the others are represented by dotted lines. The arrows indicate the directions of the changes in absorbance at the respective wavelengths. (**b**, **c**) Transient spectra induced by mixing photochemically reduced *Bs*FNR (9 μM) with (**b**) 100 μM and (**c**) 500 μM $NADP^+$. The reaction was performed in 20 mM HEPES-NaOH buffer (pH 7.0) containing dRf (0.3 μM) and EDTA (0.5 mM) at 10°C. The spectra of photochemically reduced *Bs*FNR (thick continuous line) and re-oxidized *Bs*FNR (thick dashed line) were obtained by mixing 9 μM photochemically reduced *Bs*FNR with 20 mM HEPES-NaOH buffer (pH 7.0) and 30 μM potassium ferricyanide in 20 mM HEPES-NaOH buffer (pH 7.0), respectively. Spectra for 1, 4, 9, 19, 49, 99, 199, 499 and 999 ms are shown by thin dotted lines from the bottom to the top at 450 nm. The arrows indicate the directions of the changes in absorbance at the respective wavelengths, where the dotted parts indicate that the change occurred within the first acquisition period (1 ms). The inset in (**c**) represents the time course of the changes in the A_{590} induced by mixing photochemically reduced *Bs*FNR (bottom continuous line), 100 μM $NADP^+$ (upper continuous line) and 500 μM $NADP^+$ (dashed line), respectively. The data are the average of four measurements. (**d**) Time course of the change in the A_{458} induced by mixing photochemically reduced *Bs*FNR with

$NADP^+$. The measurement conditions were the same as those in Figure 3b and c, except the $NADP^+$ concentrations were **a**, 0 μM; **b**, 100 μM; **c**, 200 μM; **d**, 300 μM; and **e**, 500 μM. The data are the average of four measurements. One standard deviation of each data point was less than 7 %. Fitted curves for a single exponential decay function based on the data at each $NADP^+$ concentration are indicated by continuous red lines. (**e**) $NADP^+$ concentration dependency of the observed rate of A_{458}. The observed rate constant at each NADPH concentration was obtained as shown in Figure 3d. One standard deviation of each observed rate constant was less than 0.05 s^{-1}.

Figure 4. (**a**) Transient difference spectra induced by mixing *Bs*Fd_{red} (40 μM) with *Bs*FNR_{ox} (10 μM) in 20 mM HEPES-NaOH buffer (pH 7.0) containing 20 mM NaCl at 10°C. The spectrum of *Bs*FNR_{ox} is shown by a thick continuous line. The spectra shown represent the differences between the spectra at 0, 1, 2, 4, 6, 9, 19, 29, 49, 99, 199 and 499 ms minus that for *Bs*Fd_{red} (40 μM) alone. The difference between the spectrum at 0 ms minus that for *Bs*Fd_{red} (40 μM) alone is shown by a thin continuous line, that at 2 ms minus that for *Bs*Fd_{red} (40 μM) alone is shown by a thin continuous line with × marks, that at 499 ms minus that for *Bs*Fd_{red} is shown by a thick dashed line and the others are represented by thin dotted lines. The directions of the absorption changes are indicated by arrows, where the dotted parts indicate that the change occurred within the first acquisition period (1 ms). (**b**) Differences between the spectra at different times and at 0 ms. The spectra induced by mixing *Bs*Fd_{red} (40 μM) with *Bs*FNR_{ox} (10 μM) in 20 mM HEPES-NaOH buffer (pH 7.0) containing 20 mM NaCl at 10°C were recorded at 0, 1, 2, 5, 10, 15, 20, 30, 50, 100, 200 and 500 ms (from bottom to the top at 410 nm). The difference in the spectrum obtained at 2 ms minus that at 0 ms is indicated by a thin continuous line with × marks, the difference in the spectrum obtained at 500 ms and that at 0 ms is shown by a thick continuous line, and the others are represented by dotted lines. The directions of the changes in absorption are indicated by arrows. (**c**) The time course of A_{600} minus A_{685}. The value of A_{600} minus A_{685} at each *Bs*Fd_{red} concentration was normalized against the value of A_{600} minus A_{685} at 0 ms. The measurement conditions were the same as those in Figure 4a, except the *Bs*Fd_{red} concentrations were 40 (○), 60 (□), 80 (△) and 120 μM (⋈). The data are the average of four to five measurements. For each dataset, a fitted single exponential curve is shown by a continuous line. Inset: the dependency of the deduced rate constants on the concentration of

BsFd_{red}. One standard deviation of each observed rate constant was less than 2 %. (**d**) Difference between the spectra at different times and at 0 ms induced by mixing *Bs*Fd_{red} (100 μM) with a mixture of *Bs*FNR_{ox} (12 μM) and *Bs*Fd_{ox} (15 μM) in 20 mM HEPES-NaOH buffer (pH 7.0) containing 20 mM NaCl at 10°C. Difference in the spectra obtained at 0, 1, 4, 9, 19, 49, 99, 199, 499 and 999 ms minus that at 0 ms is shown from the bottom to the top at 410 nm. Thick line: difference between the spectra obtained at 999 and 0 ms; thin continuous line with × marks: difference between that at 9 and 0 ms. The others are shown by dotted lines. The directions of the changes in absorption in the region are indicated by arrows. The inset represents the time course of the change in absorbance for A_{600} minus A_{685}.

Figure 1a

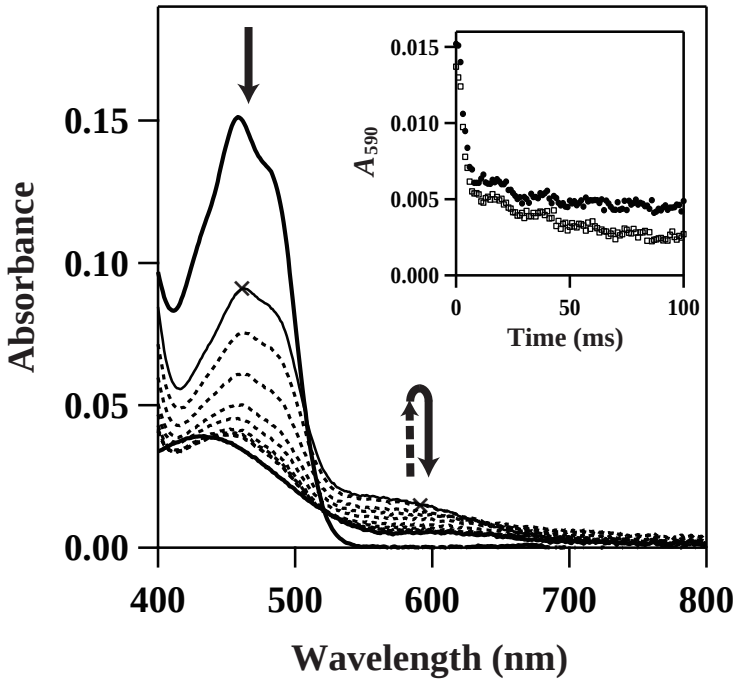
Absorbance
0.15
0.10
0.05
0.00
400
500
600
700
800
Wavelength (nm)
A_{590}
0.015
0.010
0.005
0.000
0
50
100
Time (ms)

Figure 1b

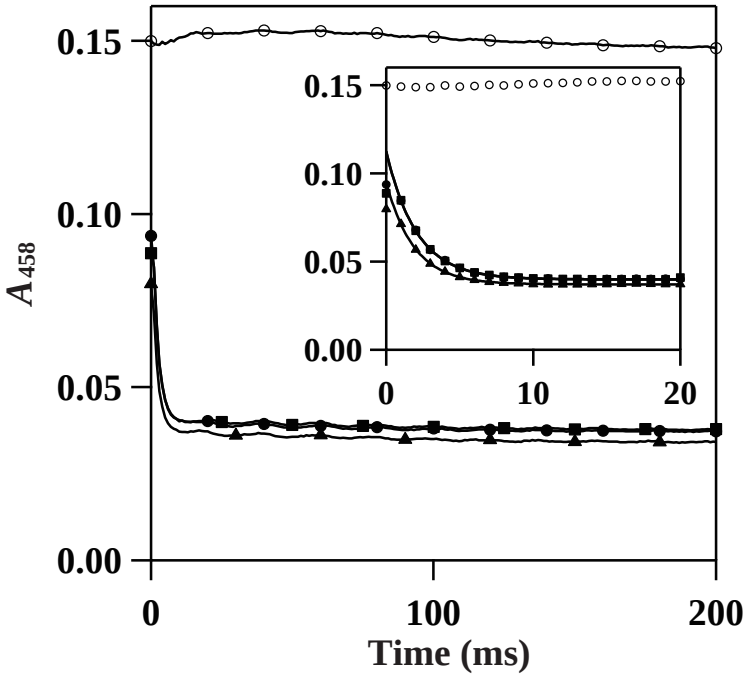

Figure 2a

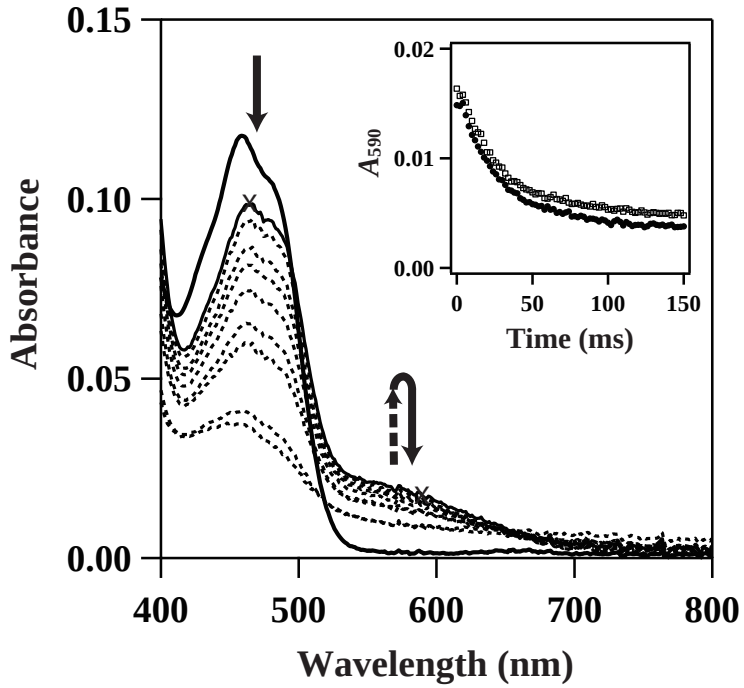
0.15
0.10
0.05
0.00
Absorbance
400
500
600
700
800
Wavelength (nm)
0.02
0.01
0.00
A_{590}
0
50
100
150
Time (ms)

Figure 2b

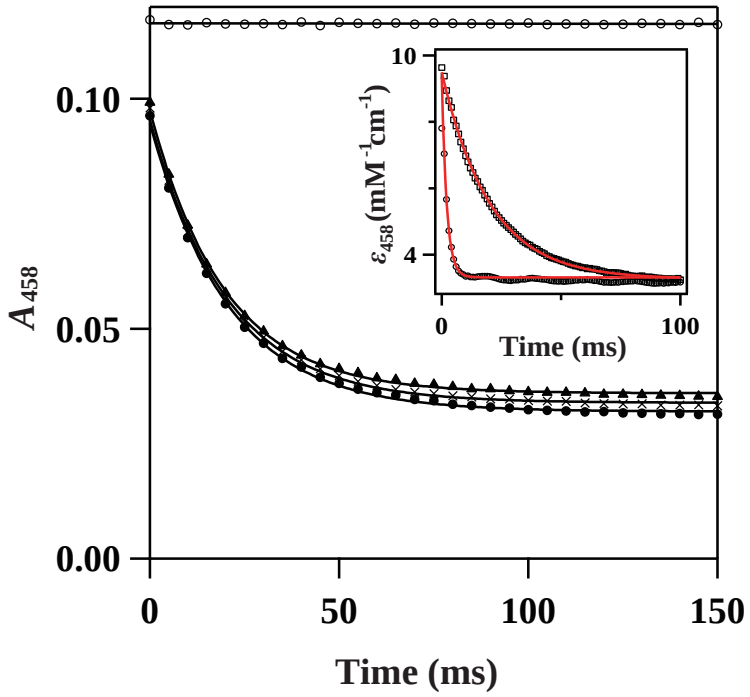
0.10
0.05
0.00
A_{458}
0
50
100
150
Time (ms)
10
4
ε_{458} (mM^{-1}cm^{-1})
0
100
Time (ms)

Figure 2c

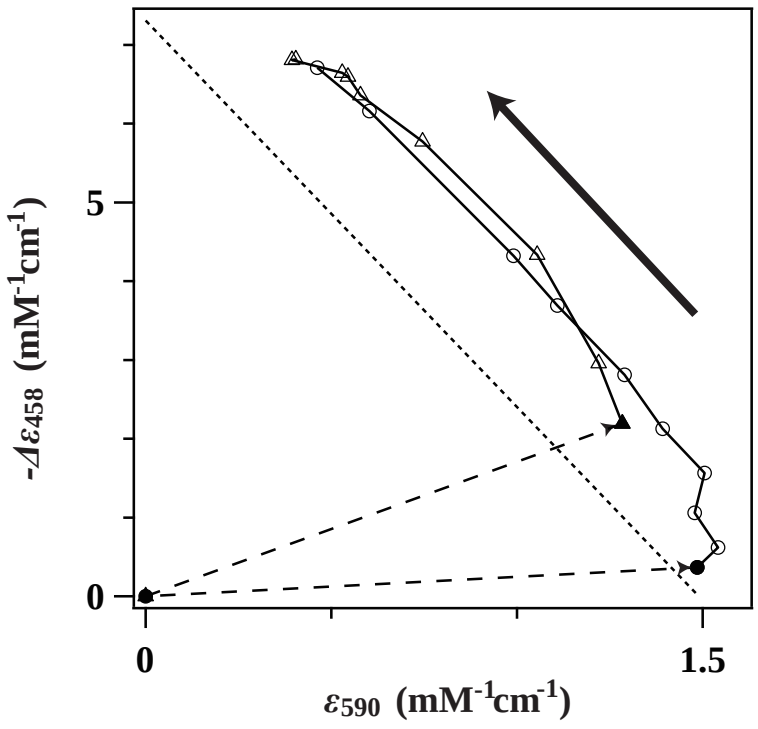

Figure 3a

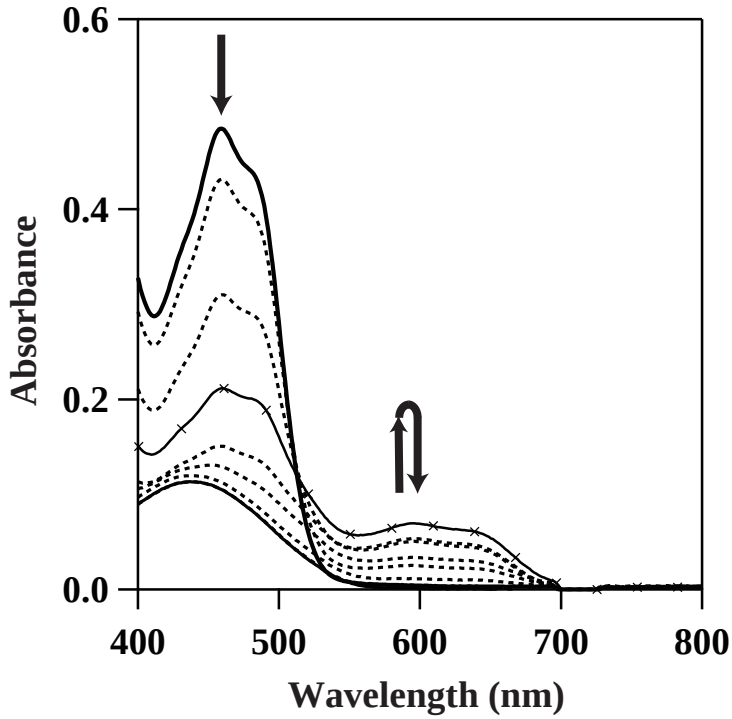

Figure 3b

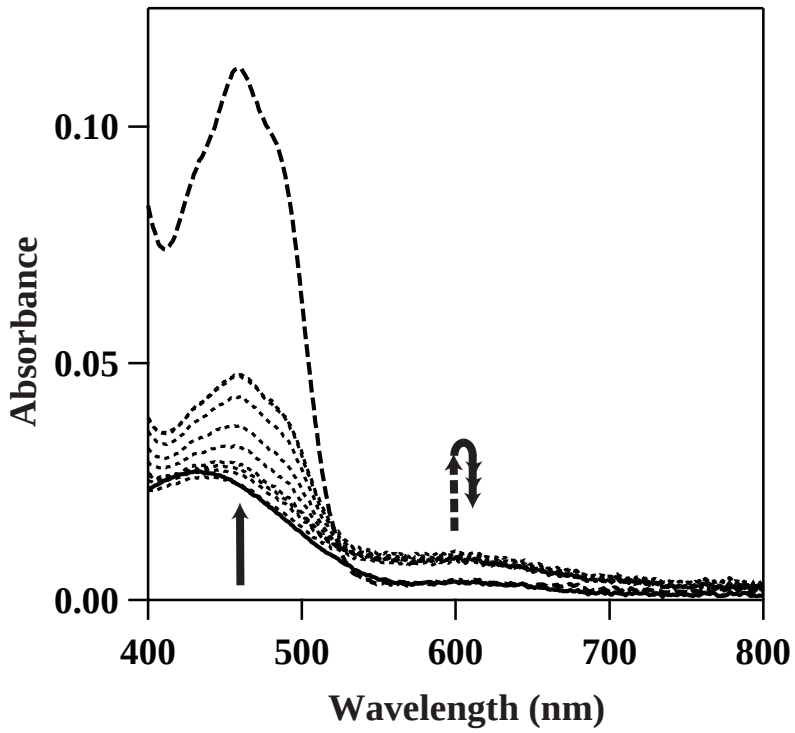

Figure 3c

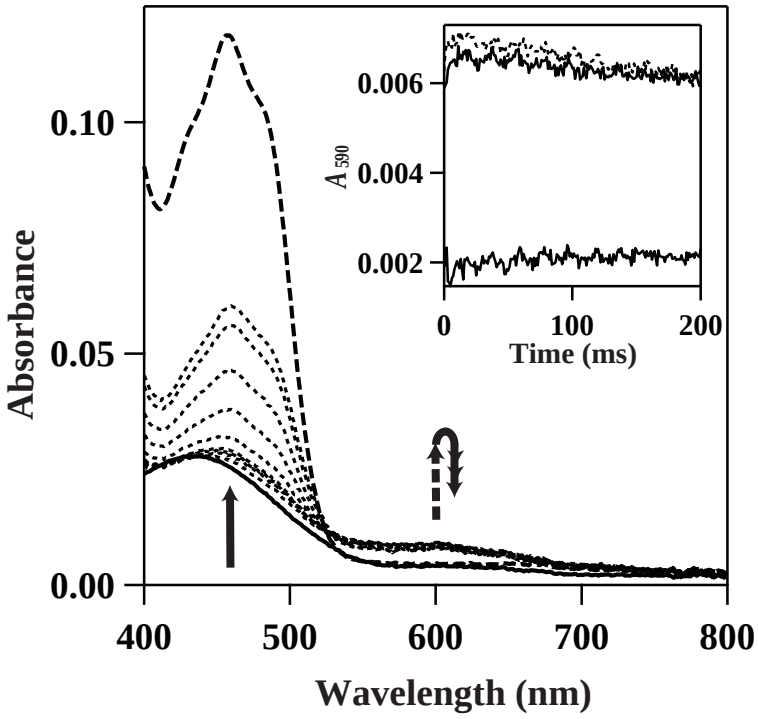
Absorbance
0.10
0.05
0.00
400
500
600
700
800
Wavelength (nm)
A590
0.006
0.004
0.002
0
100
200
Time (ms)

Figure 3d

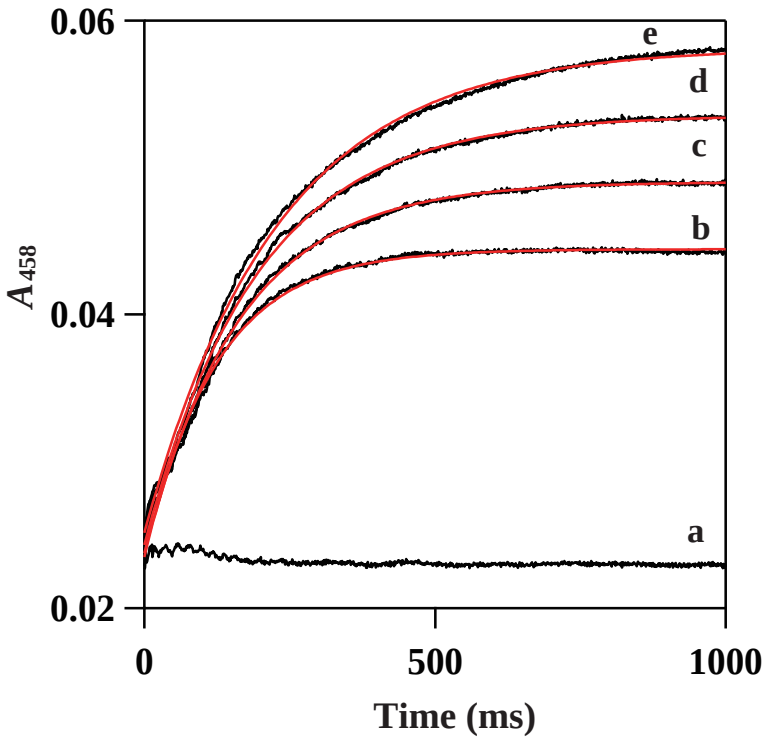

Figure 3e

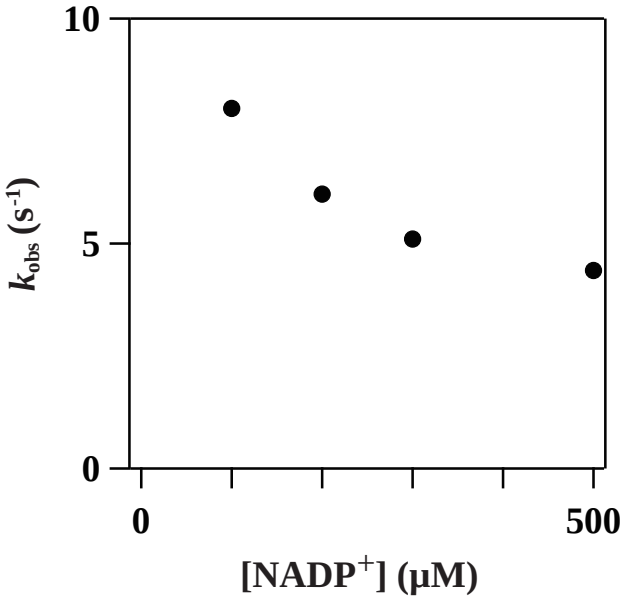

Figure 4a

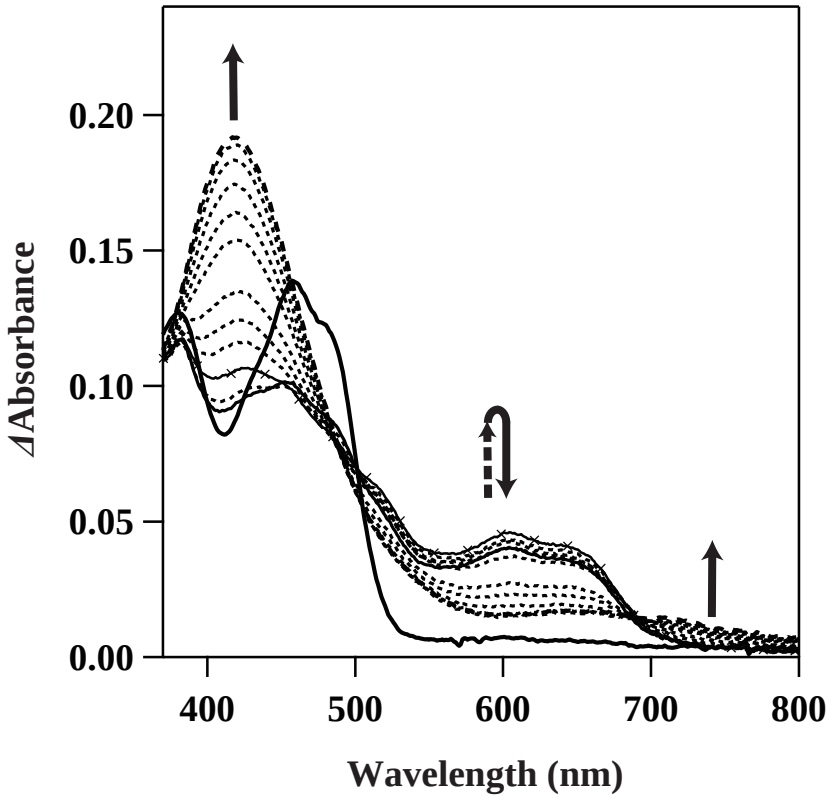
0.20
0.15
0.10
0.05
0.00
Δ Absorbance
400
500
600
700
800
Wavelength (nm)

Figure 4b

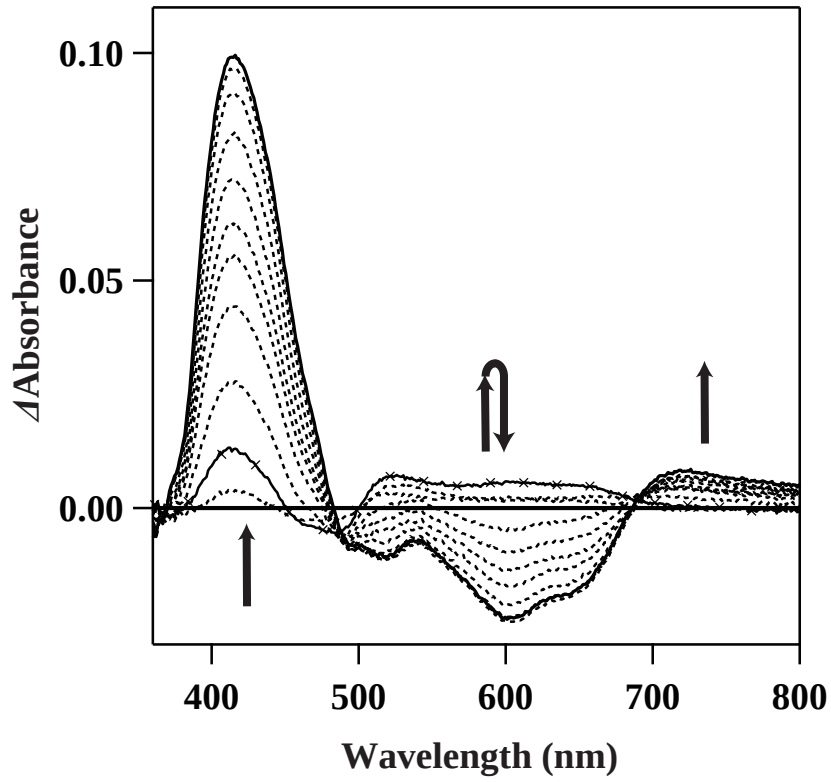

Figure 4c

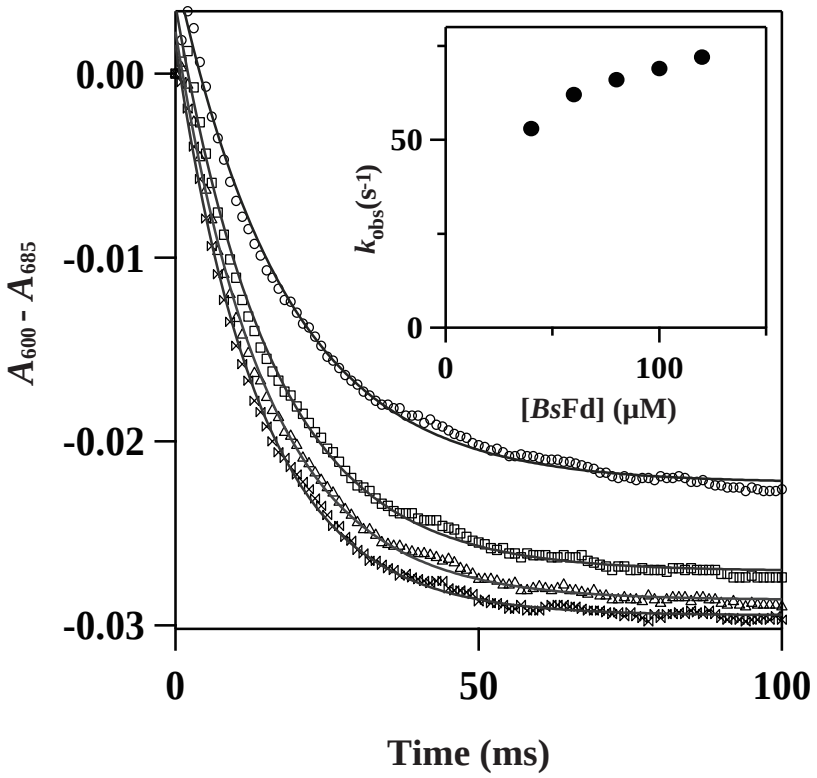
0.00
-0.01
-0.02
-0.03
A_{600} - A_{685}
0
50
100
Time (ms)
50
0
k_{obs}(s^{-1})
0
100
[*Bs*Fd] (μM)

Figure 4d

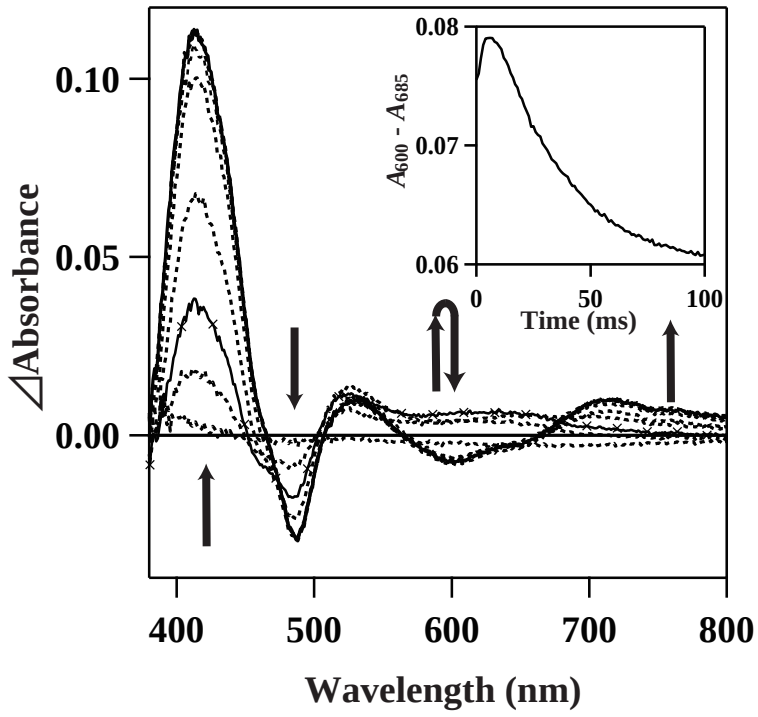
0.10
0.05
0.00
⊿Absorbance
400
500
600
700
800
Wavelength (nm)
0.08
0.07
0.06
A_{600} - A_{685}
0
50
100
Time (ms)

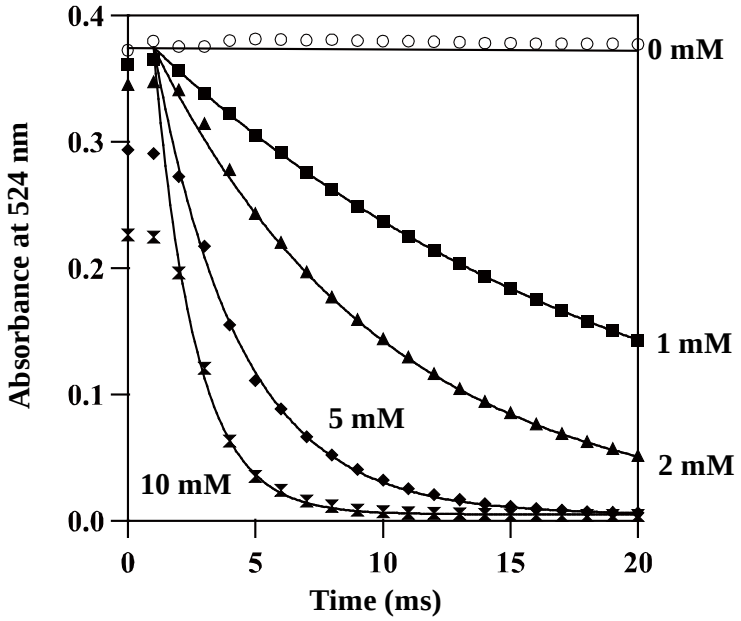

Figure S1

Transient absorbance change at 524 nm after mixing 0.1 mM DCPIP with 0-10 mM sodium ascorbate at pH 2 at room temperature. Measurement was performed utilizing a stopped-flow spectrophotometer comprised a double mixing unit (USP-SFM-D20, Unisoku Co., Ltd., Osaka, Japan) with a micro-volume cell (1 mm diameter window and 1 cm light path length), a 150 W xenon discharge lump house (USP-105-04, Unisoku Co., Ltd.) and a photodiode array detector (PK120, Unisoku Co., Ltd.). Transient spectra were corrected every 1 ms after stopping the piston motion. Fitted curves with a single exponential phase are shown as continuous lines. The time interval between the intersection point of the fitted curves at around 1 ms and the first data point on the fitted curve at 2 ms indicated that there is a 1 ms duration of the stopping the flow of solution after the stopping the piston motion and the dead time is approximately 1 ms [44]. Estimation of the dead time with the signal level of the continuous

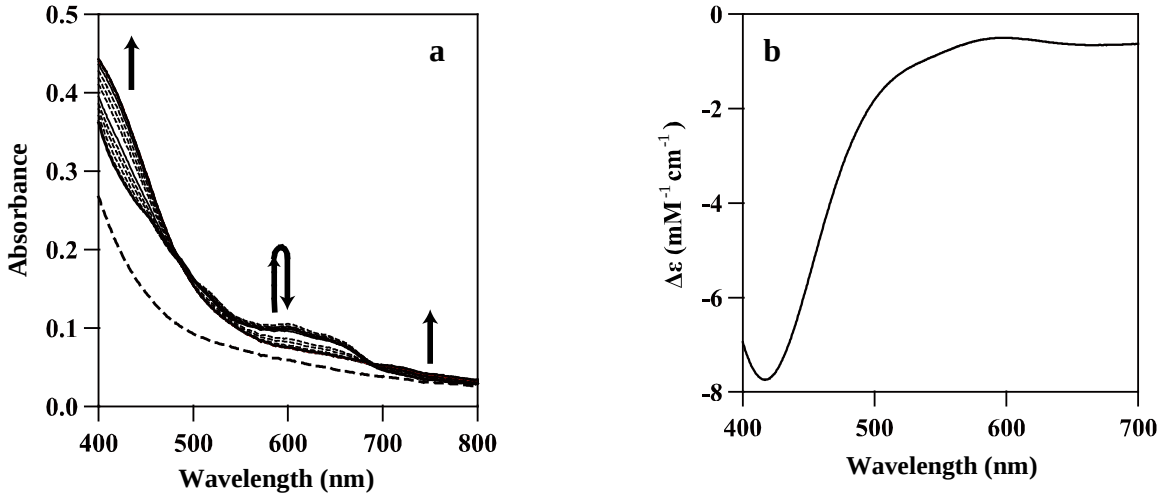

Figure S2

(**a**) Transient spectra induced by mixing dithionite-reduced *Bs*Fd (40 μM) with *Bs*FNR$_{ox}$ (10 μM) in 20 mM HEPES-NaOH buffer (pH 7.0) containing 20 mM NaCl at 10˚C under anaerobic conditions. The spectra at 1, 2, 4, 6, 9, 19, 29, 49, 99, 199, 499, 999 and 1,999 ms are represented. The spectra at 1, 9, 99, 999 and 1999 are indicated in thin continuous lines and the others in dotted lines. Spectrum of the *Bs*Fd$_{red}$ (40 μM) obtained by mixing with buffer only is represented as a thick dashed line.

(**b**) Difference spectrum of *Bs*Fd$_{red}$ minus *Bs*Fd$_{ox}$. 50 μM *Bs*Fd$_{ox}$ in 20 mM HEPES-NaOH buffer (pH 7.0) containing 25 mM NaCl was reduced by addition of excess amount of dithionite (~10 times) under anaerobic conditions at room temperature. The spectrum was measured with a double beam spectrophotometer (V-560, JASCO, Tokyo, Japan) using a solution containing all of the reagents except for *Bs*Fd$_{ox}$ as the reference.

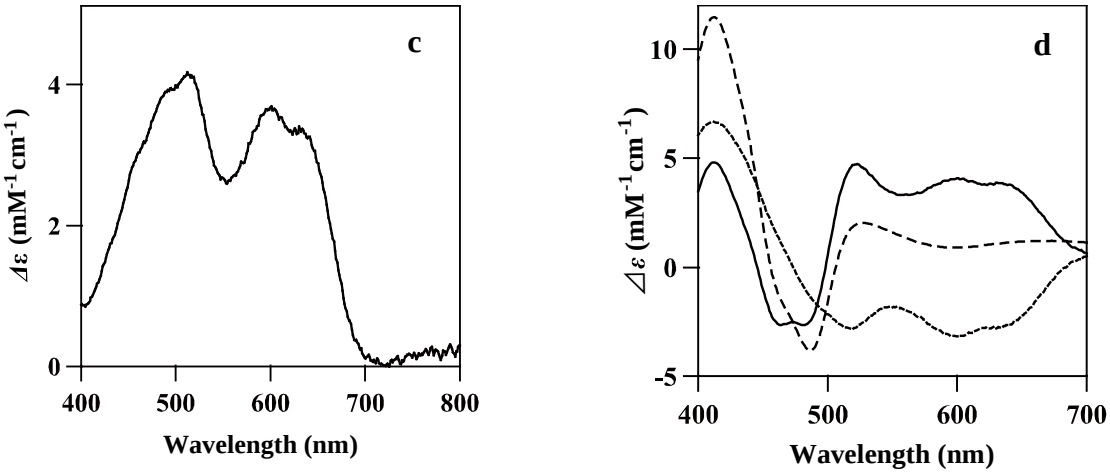

(**c**) Difference spectrum of *Bs*FNR$_{sq}$ minus *Bs*FNR$_{hq}$. Photochemically reduced *Bs*FNR (~50 μM) was reacted with 5 μM of potassium ferricyanide in 20 mM HEPES-NaOH buffer at 10°C. The difference spectrum after mixing *Bs*FNR$_{red}$ with ferricyanide minus mixing *Bs*FNR$_{red}$ with buffer is shown. We assumed that the added potassium ferricyanide was fully reduced and corresponding amount of *Bs*FNR$_{red}$ was oxidized to *Bs*FNR$_{sq}$. Absorption of ferrocyanide was ignored.

(**d**) Simulated difference spectra elicited by coupled redox reactions between *Bs*FNR$_{ox}$ and *Bs*Fd$_{red}$. The spectrum corresponding to the first reduction [<*Bs*FNR$_{sq}$ - *Bs*FNR$_{ox}$> + <*Bs*Fd$_{ox}$ - *Bs*Fd$_{red}$>], the second reduction [<*Bs*FNR$_{red}$ - *Bs*FNR$_{sq}$> + <*Bs*Fd$_{ox}$ - *Bs*Fd$_{red}$>] and the double reduction [<*Bs*FNR$_{red}$ - *Bs*FNR$_{ox}$> + 2 ×<*Bs*Fd$_{ox}$ - *Bs*Fd$_{red}$>] are represented in continuous, dotted and dashed lines, respectively. Spectra of *Bs*FNR$_{ox}$ and *Bs*FNR$_{hq}$ were obtained from [21]. Spectra of <*Bs*Fd$_{red}$ – *Bs*Fd$_{ox}$> and <*Bs*FNR$_{sq}$-*Bs*FNR$_{hq}$> were from Figure S2b, c.

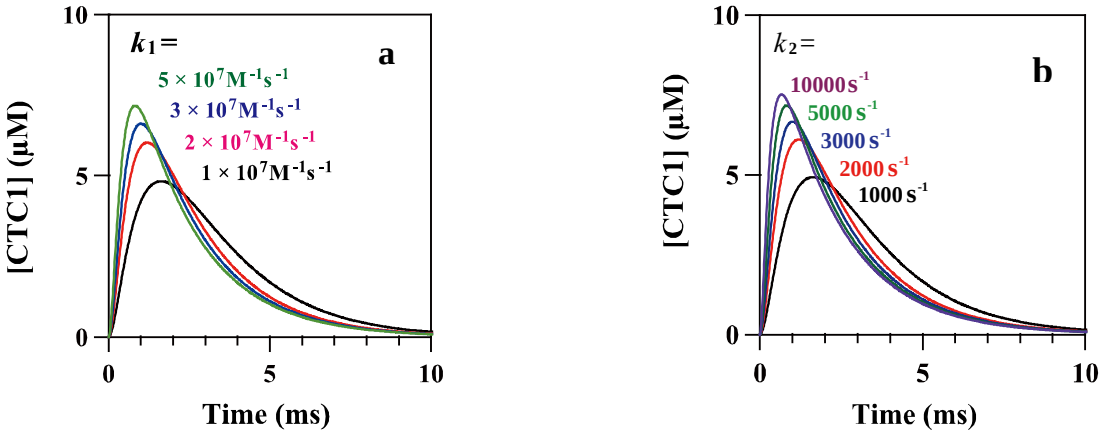

Figure S3

(**a, b**) Simulations of the time course of CTC-1 concentration in FNR_{ox} reduction by NADPH with variations of k_1 (**a**) or k_2 (**b**) values. Simulations were performed on COPASI ver. 4.11 software [50] utilizing Scheme 1 as the simulation model. Initial concentrations of FNR_{ox} and NADPH are 10 and 100 μM, respectively. Kinetic parameters are set as follow; (**a**) k_{-1} = 0 s^{-1}, k_2 = 10,000 s^{-1}, k_{-2} = 0 s^{-1}, k_3 = 500 s^{-1}, k_{-3} = k_4 = k_{-4} = k_5 = 0 s^{-1} k_{-5} = 0 $M^{-1}s^{-1}$, (**b**) k_1 = 5 × 10^7 $M^{-1}s^{-1}$, k_{-1} = k_{-2} = 0 s^{-1}, k_3 = 500 s^{-1}, k_{-3} = k_4 = k_{-4} = k_5 = 0 s^{-1}, k_{-5} = 0 $M^{-1}s^{-1}$. The values of k_1 in (**a**) and k_2 in (**b**) are indicated at the corresponding curves. The amount of CTC-1 at the first acquisition after mixing (around 1 ms) significantly decreases against those at the end of the dead time (0 ms) when k_1 is more than 3 × 10^7 $M^{-1}s^{-1}$ (in (**a**)) or k_2 is more than 5,000 s^{-1} (in (**b**)).

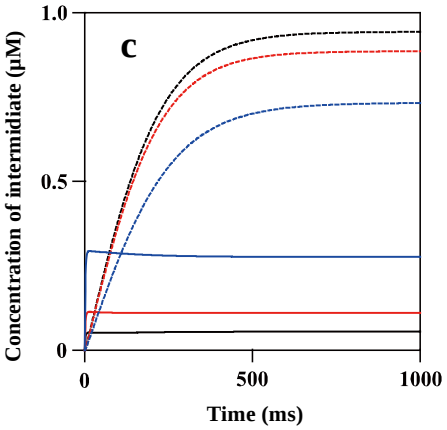

(**c**) The time course of CTC-1 (continuous lines) and FNR_{ox}-$NADP^+$ (dotted lines) concentrations in the simulations of model 1 (black lines), model 2 (red lines) and model 3 (blue lines) in Table S1 during the FNR_{red} oxidation by $NADP^+$. Simulations were performed on COPASI ver. 4.11 software [50] utilizing Schemes 1-2 as the simulation model. Initial concentrations of FNR_{red} and $NADP^+$ are 10 and 100 μM, respectively.

The $NADP^+$/NADPH concentrations used in the present study were almost saturating because the maximum CT band intensities did not depend on the $NADP^+$/NADPH concentration in the concentration range of 100–500 μM in both directions (Figs. 1a and 3c). The rate constants for the association with $NADP^+$/NADPH (k_1 and k_{-5} in Scheme 1) and the transition from MC-1/MC-2 to CTC-1/CTC-2 (k_2 and k_{-4} in Scheme 1) were estimated as being larger than 5 × 10^7 $M^{-1}s^{-1}$ and 5,000 s^{-1}, respectively, considering the dead time of the equipment and the time interval for acquisition (Fig. S3a and b). Accordingly, the minimum values of 5 × 10^7 M^{-1} s^{-1} and 500 s^{-1} for k_1 and k_{-5}, and k_{-1} and k_5, respectively, were utilized for the simulation, which corresponded to K_d values of 10 μM for NADPH and $NADP^+$. These values are large enough not to change the rate-determining step in each direction and do not significantly affected on the absorption of flavin band I as these rate constants relate to the reactions between the same redox state.

Table S1 Kinetic parameters of the simulation models

model	k_1/k_{-1}	k_2/k_{-2}	k_3/k_{-3}	k_4/k_{-4}	k_5/k_{-5}	k_6/k_{-6}
1	5×10^7/500	5,000/1000	500/10	10,000/5000	500/5×10^7	5×10^7/500
2	5×10^7/500	5,000/ **440**	500/**20**	10,000/5000	500/5×10^7	5×10^7/500
3	5×10^7/500	5,000/ **120**	500/**50**	10,000/5000	500/5×10^7	5×10^7/500

* The kinetic parameters used for the simulation with Schemes 1-2. Unit of each parameter is s^{-1} or $M^{-1}s^{-1}$. The different values in model 2 and 3 from those in model 1 are highlighted.

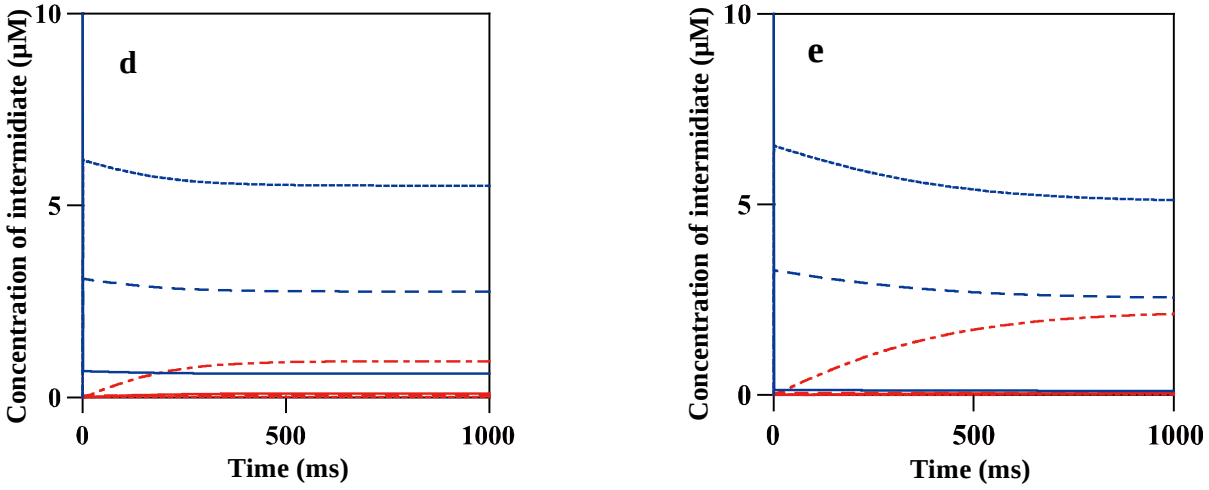

(**d, e**) Simulations of the transitions of the intermediate species after mixing (**d**) 10 μM *Bs*FNR$_{red}$ with 100 μM $NADP^+$ or (**e**) 10 μM *Bs*FNR$_{red}$ with 500 μM $NADP^+$ utilizing the kinetic parameters of the model 1 in Table S1. Simulations were performed on COPASI ver. 4.11 software [50] utilizing schemes 1-2. Blue continuous line: *Bs*FNR$_{red}$, blue dotted line: MC-2, blue dashed line: CTC-2, red continuous line: *Bs*FNR$_{ox}$, red dotted line: MC-1, red dashed line: CTC-1, red long dashed dotted line: *Bs*FNR$_{ox}$-$NADP^+$.